ON ANTARCTIC SEA ICE PRODUCTION DURING 1998-2020

A Thesis

by

JACOB SAMUEL ARNOLD

Submitted to the Graduate and Professional School of
Texas A&M University
in partial fulfillment of the requirements for the degree of

MASTER OF SCIENCE

Chair of Committee,	Alejandro H. Orsi
Committee Members,	Achim Stoessel
	Kenneth Bowman
Head of Department,	Shari Yvon-Lewis

December 2022

Major Subject: Oceanography

ABSTRACT

Antarctic sea ice production has important implications for the global Meridional Overturning Circulation. Large volumes of sea ice are produced over the Antarctic continental shelf during the winter. In some regions the associated salt rejection creates dense Shelf Water and triggers convection to the bottom layer. Multiple outflows of Shelf Water sink down the continental slope and fill the abyssal Southern Ocean

This study generates a new sea ice thickness dataset based on the National Ice Center ice charts. Compared to previous estimates, the average thickness of the new dataset is greater than the zero ice freeboard approach, lower than a radar altimetry-based snow climatology approach, and in agreement with the GIOMAS model.

Sea ice thickness is combined with sea ice motion data to calculate sea ice production in sixteen gated sectors of the Antarctic shelf. The estimated mean sea ice production in all sixteen Antarctic shelf sectors is 2849 km^3/year. Just the two most productive areas account for 63.5% of the total: Ross (1010 km^3/year) and Southern Weddell (800 km^3/year); three areas with moderate production account for another 23.5%: Prydz , Bellingshausen, and Amundsen; and the remaining 17.5% is derived from multiple low production areas. Four sectors represent net sinks of sea ice volume: West Weddell, Marguerite, Bowman, and Adelie; but combined only reduced total mean sea ice production by 5.5%.

Salinity timeseries for each shelf sector are calculated from the estimated amount of salt rejected during sea ice production and estimates of meltwater inputs from adjacent continental ice. With a local meltwater input of 91.5 Gt/year to the Ross Sea, the sea ice production indicates a winter convective period of ~200 days; however, the addition of 518 Gt/year from upstream would shorten it to ~100 days. A hypothetical meltwater input of 700 Gt/year to the Ross Sea would be sufficient to intermittently shut down local convection. In contrast, the Southern Weddell produces Shelf Water each year despite the local meltwater input of 159 Gt/year and the 241 Gt/year from upstream. About 500 Gt/year of total meltwater input to the Weddell Sea would be required to intermittently stop convection.

DEDICATION

This work is dedicated to my wife, Kaitlyn Arnold. She is the epitome of supporting wife, loving mother, and wonderful friend. Without Kaitlyn this would not have been possible.

ACKNOWLEDGEMENTS

The completion of this thesis is an important milestone in a transformational process. Dr. Alejandro Orsi agreed to be my advisor in oceanography despite my sociology undergraduate degree (a considerably different field). With his carefully tailored encouragement, guidance, and motivation I gained competence in the skills necessary to research physical oceanographic phenomena and present the results to others. Thank you, Dr. Orsi for providing this opportunity and for your patience through this process. I must also thank my committee members, Dr. Achim Stoessel and Dr. Kenneth Bowman for the immense amount of patience and kind feedback they have provided which contributed significantly to this work.

My wife, Kaitlyn is a huge part of my life and has provided the emotional (and financial) support necessary to see me through this part of my education. Kaitlyn also provides the freedom to escape from school for a time, putting in extra work to allow me to go motorcycling, mountain biking, and camping. Our son, Theodore, was born just ten days before the start of my first graduate semester and his playful nature and general excitement about life encourages me daily. Thank you, Kaitlyn and Theo for your perpetual daily love and support, I owe much of my achievement to you.

My parents, Jack and Kay Arnold have never failed to provide encouragement and support throughout my education, during both struggling and thriving periods. Thank you for your support and for raising me to value working hard and enjoying the work that I complete.

Friendships are the real treasures we collect through life. From spontaneous camping road trips to daily talks about mutual research and coding frustrations, my friends have added a level of joy to this process that I would not have expected. Thank you, Dylan Schlichting and the many other friends I've made during these years.

Finally I must thank the oceanography department which has facilitated this work by providing funding as a teaching assistant, allowing me to gain experience teaching a wide array of classes, and for providing financial support through numerous scholarships and fellowships.

CONTRIBUTORS AND FUNDING SOURCES

This work was supervised by a thesis committee consisting of Professor Alejandro Orsi and Professor Achim Stoessel of the Department of Oceanography and Professor Kenneth Bowman of the Department of Atmospheric Sciences. Graduate study was supported by teaching assistantships through the Department of Oceanography at Texas A&M University as well as the National Science Foundation S-STEM scholarship, the Louis and Elizabeth Scherck scholarship, the Ralph Rayburn ’69 scholarship, and the Robert O. Reid Oceanography Fellowship.

NOMENCLATURE

AASW	Antarctic Surface Water
SAF	Subantarctic Front
ACC	Antarctic Circumpolar Current
AAIW	Antarctic Intermediate Water
SW	Shelf Water
CDW	Circumpolar Deep Water
AABW	Antarctic Bottom Water
MOC	Meridional Overturning Circulation
SAM	Southern Annular Mode
SIE	Sea Ice Extent
SIC	Sea Ice Concentration
SIV	Sea Ice Volume
SIT	Sea Ice Thickness
SIP	Sea Ice Production
SIM	Sea Ice Motion
EUMETSAT	European Organization for the Exploitation of Meteorological Satellites
NSIDC	National Snow and Ice Data Center
ASI	ARTIST Sea Ice algorithm
ICESat	Ice, Cloud, and Elevation Satellite

ZIF	Zero Ice Freeboard
OLM	One Layer Method
ESCS	Envisat and CryoSat-2
GIOMAS	Global Ice-Ocean Modeling and Assimilation System
ULS	Upward Looking Sonar
ASPeCt	Antarctic Sea Ice Processes and Climate
NIC	U.S. National Ice Center
NOAA	National Oceanic and Atmospheric Administration
ESRI	Environmental Systems Research Institute
S	Ice Chart Stage of Development
C	Ice Chart Partial Sea Ice Concentrations
SOD	Stage of Development-based Sea Ice Thickness
SIVT	Sea Ice Volume Transport
nSIM	Perpendicular Sea Ice Motion
ΔSIV	Change in Interior Volume
WTW	Winter Thermostad Water

TABLE OF CONTENTS

Page

LIST OF FIGURES

Page

LIST OF TABLES

Page

CHAPTER I

INTRODUCTION

Much of the Antarctic sea ice is produced during the winter in the many coastal polynyas found around the Antarctic continent (Figure 1) (Massom et al., 1998). Over these polynyas strong and extremely cold katabatic winds blow outward from tall Antarctic ice sheets, extracting latent heat from the surface of the ocean that freezes to form sea ice and delivers brine to the upper waters (Gordon, 2009). Newly formed sea ice is subsequently blown away from the continental shelf leaving an area of open water in which the process begins anew. The constant creation and offshore transport of sea ice provides freshwater to the surface layer of the Southern Ocean offshore and salt over the continental shelf. Tamura et al. (2008) estimate that about 10% of the total volume of sea ice covering the Southern Ocean each year is produced within thirteen major coastal polynyas occupying only about 1% of the maximum area covered with sea ice by the end of winter. Total sea ice production over the entire Antarctic shelf is likely much greater from the thermodynamic growth and perpetual opening and refreezing of leads in the pack ice (Nicholls et al., 2009).

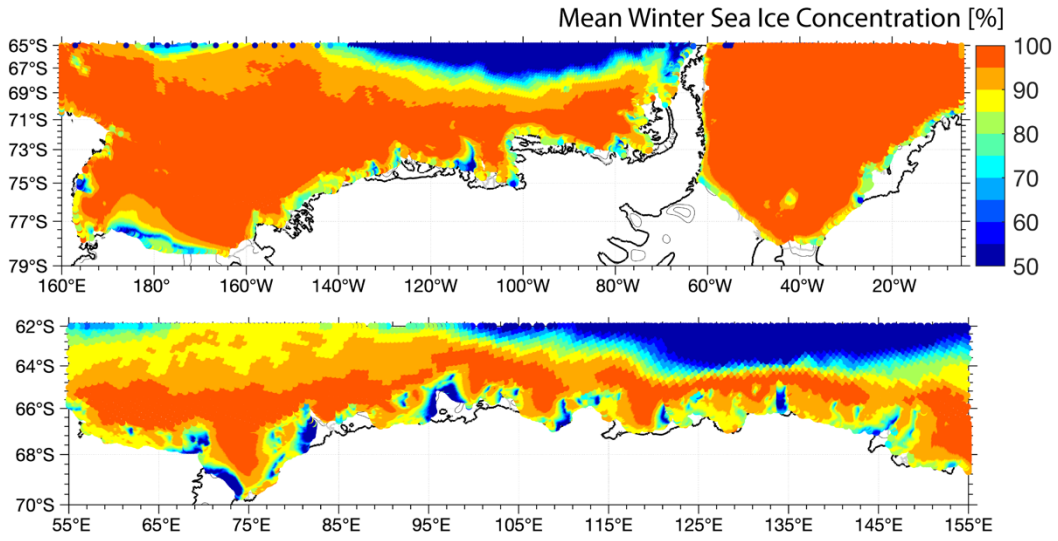

Figure 1. Mean winter (June 16 – September 15) sea ice concentration in the Antarctic. Coastal polynyas are found in the green and blue areas near the coast where there is open water during a portion of the winter.

Offshore freshwater (sea ice) transport and inshore salt rejection have important implications for the stability of the water column. In the oceanic domain, where the bulk sea ice volume melts, cold and fresh Antarctic Surface Water (AASW) is found (Whitworth III et al., 1998). Northward Ekman transport of AASW past the Subantarctic Front (SAF) of the Antarctic Circumpolar Current (ACC) contributes to the formation of Antarctic Intermediate Water (AAIW) (Deacon, 1937; Sloyan & Rintoul, 2001), apparent as an intermediate salinity minimum throughout the southern hemisphere. Over certain weakly stratified Antarctic shelf areas, the addition of salt to near-freezing AASW is sufficient to form much denser Shelf Water (SW), triggering convection (Figure 2). SW tends to accumulate in the bottom layer of numerous cross-shelf troughs (Gill, 1973). When SW piles up above the sill depths of these troughs it spills over the

continental slope, entraining Circumpolar Deep Water (CDW) (Jacobs et al., 1970) to form the Antarctic Bottom Water (AABW) that fills the abyssal layer of the Southern Ocean. Northward transport of AABW along a system of deep western boundary currents completes the lower limb of the global Meridional Overturning Circulation (MOC) (Gordon, 2009). Therefore, variability in the volume of sea ice produced within the Antarctic shelf has a significant impact on climate by influencing global oceanic circulation and stratification.

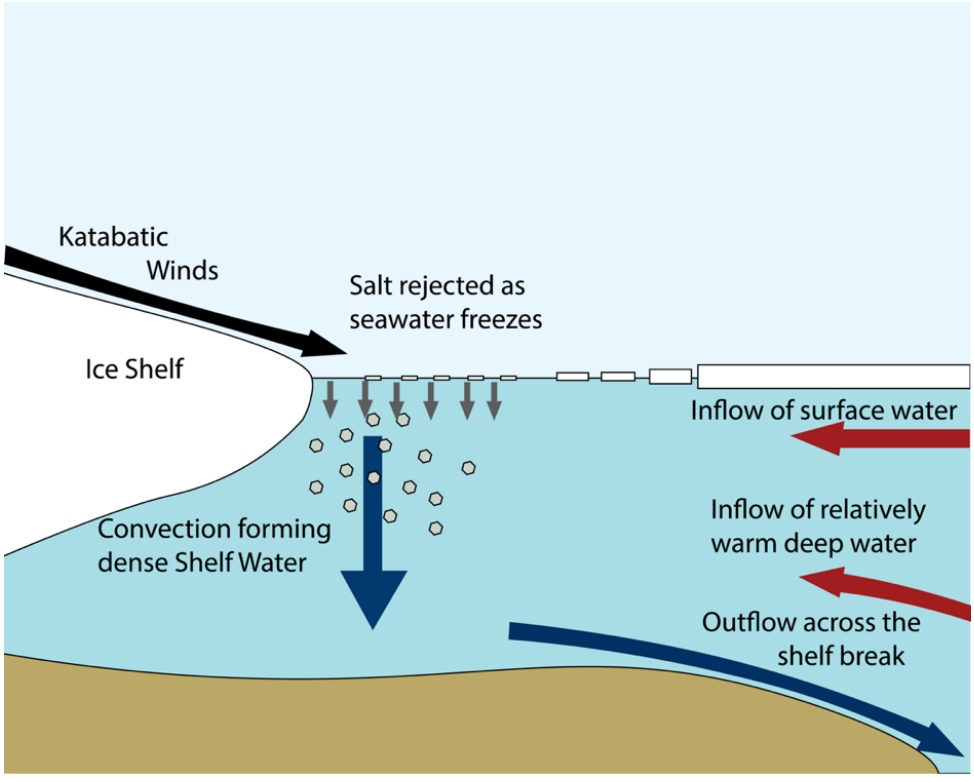

Figure 2. Schematic of a coastal polynya. Constant salt rejection can destabilize local stratification leading to outflow of dense water off the Antarctic shelf.

In recent decades, widespread freshening of multiple waters with Antarctic origin has been extensively reported: AASW (Hellmer et al., 2011; Jacobs et al., 2002), AAIW (Helm et al., 2010; Wong et al., 1999), SW (Jacobs et al., 2002; Jacobs & Giulivi, 2010), and AABW (Johnson et al., 2008; Purkey & Johnson, 2013; Rintoul, 2007). In the Ross Sea some of the AABW and SW freshening has been attributed to increased freshwater injection from melting glaciers and ice shelves in the Amundsen Sea (Jacobs & Giulivi, 2010) and to increasing Southern Annular Mode (SAM) index (Thoma et al., 2008). Relatively little is currently known about the impact of variability in regional sea ice production on these trends.

Sea Ice Extent (SIE), the sum of all areas with at least 15% Sea Ice Concentration (SIC), has been carefully tracked since the addition of passive microwave sensors to satellite platforms in the late 1970s. In the Arctic, yearly SIE shrunk at a rate of -3.7%/decade (Cavalieri & Parkinson, 2012). In contrast, Antarctic SIE slowly grew (1%/decade) until 2014 before plummeting to its lowest value in the 40 year record. The pace of the latter decline has varied regionally (Parkinson, 2019). SIE data alone does not necessarily reflect on Sea Ice Volume (SIV) variability.

Recent advances in satellite technology offer the potential to track Sea Ice Thickness (SIT) on hemispheric scales, although current results are highly variable. Kurtz and Markus (2012) showed Antarctic thinning trends in Summer (-0.3 m/decade) and Spring (-0.2 m/decade) during 2003-2008, which combined with the expanding SIE trend, still led to net summer growth in SIV. Spring thinning overshadowed the areal increase to result in net decay in SIV. In contrast, Morgan (2011) estimated increasing

trends in both SIT and SIV during 2000-2010. Modeled SIT products show increasing SIV during 1980-2008 (Massonnet et al., 2013) and 2003-2013 (Liao et al., 2022) followed by a sharp decrease beginning in 2014 (Liao et al., 2022).

Most studies of Antarctic sea ice variability have focused on the vast oceanic areas of the Southern Ocean. However, estimating the net Sea Ice Production (SIP) and its variability over the continental shelf is key to better understanding where, how likely, or how intense near-boundary convection takes place around Antarctica (Killworth, 1977). Furthermore, it might link anomalies from SIP variability over certain Antarctic continental shelf segments to the observed decadal freshening of AABW in adjacent basins.

1.1 Objectives

The goals of this project are: 1.) to create a new Southern Ocean SIT dataset using operational ice charts and SIC data; 2.) to compare this new SIT dataset with altimetry and model SIT products; 3.) to use the new SIT dataset along with Sea Ice Motion (SIM) to calculate SIP in sixteen Antarctic coastal sectors; 4.) to use SIP timeseries along with documented and hypothetical glacial meltwater inputs to estimate the sectors' salinity timeseries; and 5.) to evaluate the potential for local SW production and the duration of local convective periods.

1.2 Hypothesis

Variability in sea ice production over the Antarctic continental shelf has a significant influence on the intensity and modes of near-boundary convection.

1.3 Sea Ice Production

Regional estimates of SIP are fundamental to studies of SW variability. SIP accounts for all thermodynamic growth of sea ice while neglecting dynamic thickening that results from combining already existing volumes. Heat budget analyses in thin ice areas (<0.2 m) using the "thin ice thickness" algorithm applied to passive microwave data have rendered SIP rates at the most well-known polynyas (Comiso et al., 2011; Drucker et al., 2011; Martin et al., 2007; Nihashi & Ohshima, 2015; Tamura et al., 2016; Tamura et al., 2008). The relatively coarse (6.25 km – 25 km) resolution of the source passive microwave data, however, leads to SIP underestimates in key areas like the Weddell Sea (Tamura et al., 2008), where persistent narrow polynyas contribute significantly to the global production of AABW (Orsi et al., 2002). The heat budget approach is also limited to regions with consistently thin ice (i.e. the polynya areas), thus not capturing thermodynamic SIV growth at pervasive opening and refreezing leads found over the rest of the shelf. The heat budget approach also neglects any local freshwater input from sea ice melt (negative SIP contributions).

By combining remote sensing SIC and SIM with "empirical" SIT this study pursues a hybrid approach to calculating SIP rates inshore of flux gates spanning sixteen shelf sectors around Antarctica (Comiso et al., 2011; Orsi & Webb, 2022; Wiederwohl,

2012). The next chapters describe the datasets (Chapter 2) and methods (Chapter 3) employed to estimate the 1998-2020 timeseries of SIP over the Antarctic shelf (Chapter 4); followed by comparison to previous estimates derived from the "thin-ice thickness" algorithm and from using modelled SIT at the flux gates, and the assessment of their potential influence on regional upper waters stability and property variability. Chapter 5 reviews the most relevant results from this study.

CHAPTER II

DATA

2.1 SIC

Since 1978 the European Organization for the Exploitation of Meteorological Satellites (EUMETSAT) Ocean and Sea Ice Satellite Application Facility (OSISAF) generate daily SIC data with 25 km resolution by applying their own algorithm to brightness temperature data from multiple satellite records and validating against analyst-produced sea ice charts (Tonboe et al., 2016; Tonboe & Nielsen, 2010). Their SIC dataset is publicly available at the National Snow and Ice Data Center (NSIDC).

The University of Bremen Institute of Environmental Physics Sea Ice Remote Sensing Laboratory has independently produced SIC data with higher resolution (3.125 km polar stereographic grid) since 2002 by applying the ARTIST Sea Ice (ASI) algorithm (Spreen et al., 2008) to brightness temperature data from the Advanced Microwave Scanning Radiometer for EOS (AMSR-E) aboard NASA satellite Aqua, and from the Advanced Microwave Scanning Radiometer 2 (AMSR-2) aboard JAXA satellite GCOM-W1 (Melsheimer, 2019). Their SIC dataset is publicly available at the University of Bremen's sea ice remote sensing archive.

2.2 SIM

Since 1978 the NSIDC produces daily SIM data in the Antarctic with a 25 km resolution by tracking displacement of sea ice with similar features via satellite

microwave radiometry. Their SIM dataset is publicly available at NSIDC (Tschudi, 2019).

2.3 SIT

Antarctic sea ice cover is complex. Small leads tend to open and close in response to changing divergent and convergent wind forcing, colliding floes form ridges with variable thickness and width, snow accumulates at different rates on top of sea ice and could even weigh it down below the sea surface, and icebergs drifting with subsurface currents easily cut through the ice pack (Doronin & Kheisin, 1977). Determining SIV variability in relatively large regions requires robust information about the average areal coverage and thickness of each type of sea ice present in those regions.

Because there is currently no method capable of directly measuring the detailed variations in SIT on large scales, SIV estimates must rely on model output or inferred proxy measurements of area-mean SIT. Altimetry data, for example, are used to estimate sea ice freeboard, i.e. the thickness of sea ice above the sea surface (Figure 3), from which total SIT can be derived. These area-mean SIT estimates in the Antarctic are particularly difficult to make due to the poorly measured thickness and density of the overlaying snow layer and the lack of in situ SIT measurements to validate them. Nevertheless, a few remote sensing methods and numerical models partially cope with the above challenges.

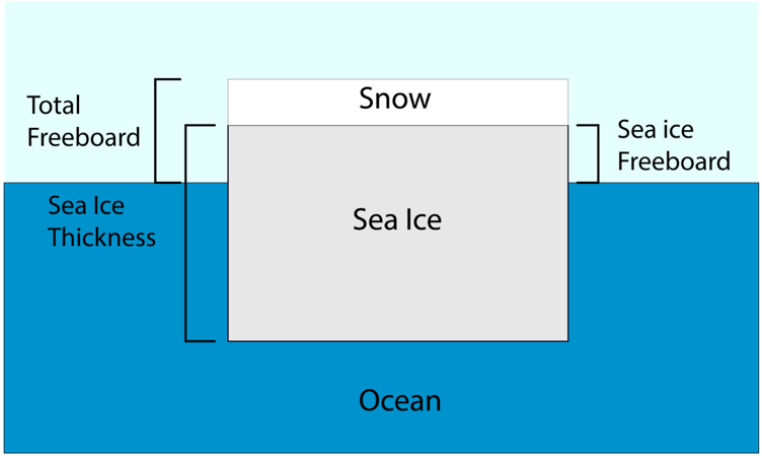

Figure 3. Example cross section of sea ice. Snow loading on the sea ice complicates SIT retrieval from satellite altimetry.

2.3.1 ICESat SIT

NASA's Ice, Cloud, and Elevation Satellite (ICESat) was launched in January 2003, equipped with a 3-laser Geoscience Laser Altimeter System (GLAS) on a planned 5-year mission. The first altimeter failed after only 36 days prompting a revision of the mission. The laser was run during 1-3 campaigns per year for a total of approximately 30 days, thus providing global coverage for only a portion of the winter, spring, and fall (Schutz et al., 2005). The final laser altimeter became unresponsive in 2009 and attempts to regain control were terminated in February 2010 (DeWitt, 2010). In total, ICESat operated for 13 missions for a total of 466 days over the course of 6 years. Its successor, ICESat-2, was launched in 2018 with the Advanced Topographic Laser System (ATLAS) projecting 6 beams compared to only one at a time in the GLAS, and capable of continuous recording (NASA, 2019).

Kurtz and Markus (2012) applied the Zero Ice Freeboard (ZIF) approach using ICESat data to estimate Antarctic SIT, which assumes that all sea ice is weighted down by snow all the way to the sea surface level. Though considered reasonable for thin ice, this method significantly underestimates thicker ice types that have sufficient buoyancy to support their snow load at levels well above the sea surface. Thus the ZIF method is likely to render a lower limit of an area's SIT. A different One Layer Method (OLM) (Kern et al., 2016) does not rely on snow depth data, but sea ice and snow are treated as a single lighter layer based on fixed seasonal ratios (R) of freeboard to snow depth. An updated OLM (Li et al., 2018) includes a dynamic R determined from linear relationships between snow depth, SIT, and freeboard; and more recently the OLMi (Xu et al. 2021), which includes a term to subtract the snow depth from the total density-reduced SIT, was applied to both ICESat and ICESat-2 data.

2.3.2 Envisat and CryoSat-2 SIT

Launched in March 2002, Envisat was the largest earth observing satellite ever built carrying instruments for observation of land, ocean, ice, and atmospheric variables. This included the Radar Altimeter System (RA-2) to continually measure global surface elevations with an accuracy of a few centimeters (Resti et al., 1999). Communication with Envisat was lost in April 2012 terminating its mission. CryoSat-2 was launched in April 2010 continuing the polar focused mission planned for the original CryoSat, which was lost because of a launch failure. CryoSat-2 carries the SAR Interferometer Radar Altimeter (SIRAL) and remains in operation to this day.

Antarctic sea ice freeboard and SIT were estimated from both Envisat and CryoSat-2 (ESCS) measurements (Hendricks, 2018a, 2018b). Freeboard is converted to SIT using a snow thickness climatology to approximate the weight of the snow layer. This method assumes that the radar signal reflects at the snow-ice interface (Paul, 2017), which is true for laser altimeters but not for radar signals since they reflect from somewhere within the snow layer (Willatt et al., 2009). Therefore, this method leads to a general overestimate of SIT, especially where snow is thick (Kacimi & Kwok, 2020). To minimize this problem Kacimi and Kwok (2020) used the difference between CryoSat-2 and ICESat-2 as an estimate of the snow depth. Since the overlapping time between these two platforms is only a few years, this approach is still incapable of providing any long-term insight on Antarctic SIT variability, but it will likely play an important role in future years.

2.3.3 Numerical modeling products

Ocean-sea ice models forced by atmospheric reanalysis data produce global SIC, SIT, and SIM. Assimilation of SIC data has been successfully applied to improve modeled SIT products in the Arctic (Lindsay & Zhang, 2006; Lisæter et al., 2003; Schweiger et al., 2011) and in a few Antarctic cases (Massonnet et al., 2013; Shi et al., 2021). The Global Ice-Ocean Modeling and Assimilation System (GIOMAS) consists of the Parallel Ocean Program and the Thickness and Enthalpy Distribution (TED) sea ice model (Zhang & Rothrock, 2003). It produced reliable SIT data in the Weddell Sea (Shi et al., 2021) and showed global SIV variability (Liao et al., 2022). It also rendered

winter underestimates of SIT compared to ESCS data, which is in turn a significant overestimate. Future assimilation of Antarctic SIT products has the potential to further improve modeled sea ice properties (Liao et al., 2022; Mu et al., 2020; Shi et al., 2021).

2.3.4 Moorings and Ship Observations

While moored Upward Looking Sonars (ULS) located well below the sea surface have provided long-term observations of SIT in several places of the Arctic, just a handful of ULSs have been deployed over the Antarctic shelf (Strass & Fahrbach, 1998; Worby et al., 2001). Thus, available Eulerian measurements of Antarctic SIT are inadequate to validate gridded area-averages (Kacimi & Kwok, 2020) derived from the above methods.

The Antarctic Sea Ice Processes and Climate (ASPeCt) program was founded by the Scientific Committee on Antarctic Research to assemble sea ice data from icebreakers. Ship observations typically include estimates of concentration, thickness, floe size, and snow cover of the sea ice pack. Over 21,000 records from 81 voyages exist in the ASPeCt dataset over the years 1981-2005 covering much of the Southern Ocean (Worby et al., 2008). However, ships generally transit through regions with the least imposing forms of sea ice and primarily during the austral summer months. This results in biasing the ASPeCt SIT data toward thin and low concentration summer sea ice, i.e. not entirely comparable to satellite-derived SIT, and therefore of little use while validating independent long-term large-scale area-mean SIT datasets (Kacimi & Kwok, 2020).

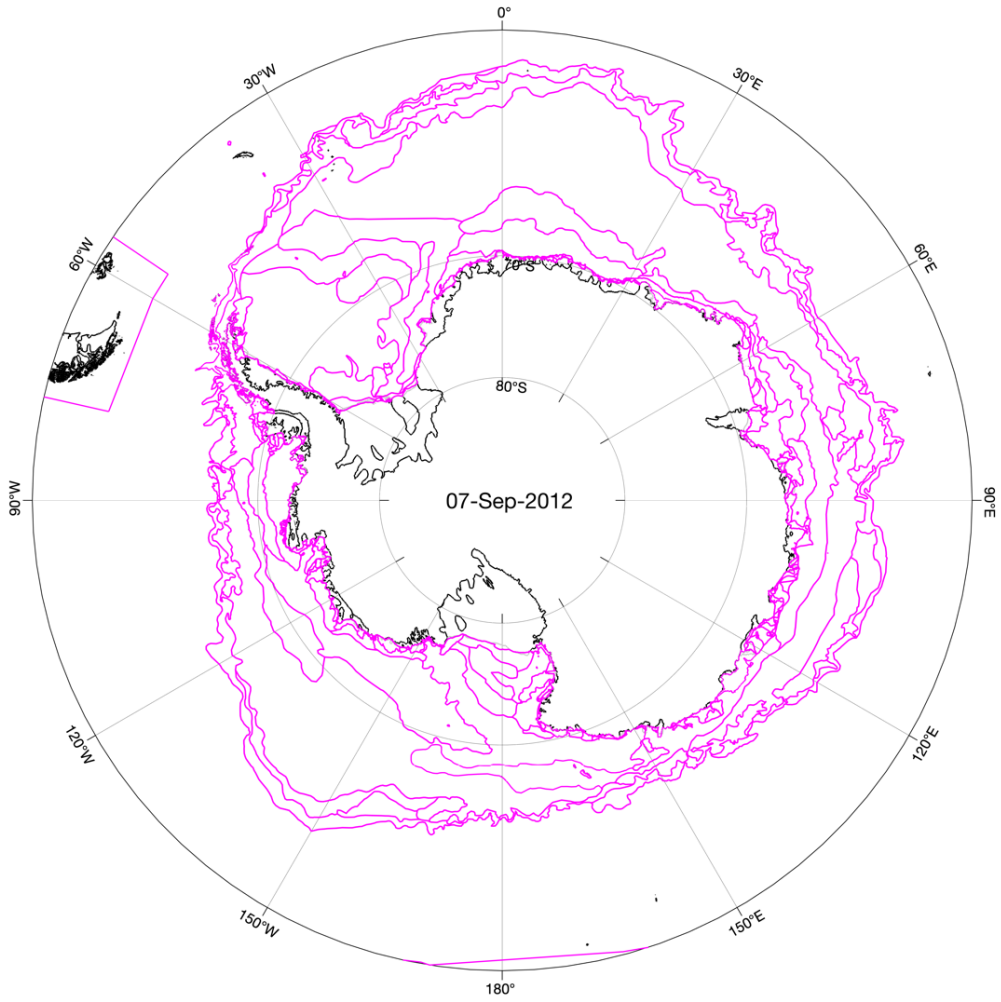

Figure 4. Example NIC ice chart polygons. Each polygon is traced around areas of similar sea ice with up to 4 varieties of ice described in that polygon.

2.3.5 NIC Ice Charts

The U.S. National Ice Center (NIC) operates as a joint agency with leadership and oversight from the U.S. Navy, U.S. Coast Guard, and the National Oceanic and Atmospheric Administration (NOAA). Special analysts at the NIC undergo comprehensive training and apprenticeship periods before being qualified to generate ice datasets, like Arctic and Antarctic icebergs and sea ice products. Weekly ice charts

produced by the NIC since 1972 in the Arctic and 1973 in the Antarctic were originally intended to support ship navigation. They are composed of polygons traced by the specialists around areas found to have similar ice characteristics (Figure 4). Using the international standard SIGRID "egg code" (Figure 5), each polygon contains information on the total SIC (Ct), partial concentration (Ca-d), stage of development (Sa-d), and flow size (Fa-d) of up to four SIT categories.

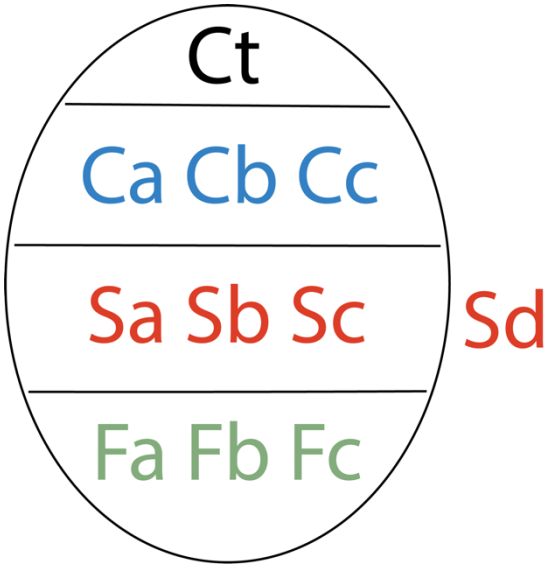

Figure 5. The SIGRID "egg code" including all components that can be used to define the ice within an NIC ice chart polygon.

To produce these sea ice charts, NIC analysts assimilate data from passive and active microwave radiometers, visual and infrared imagery, and model output. Active microwave radiometers (RADARSAT-1, RADARSAT-2, ENVISAT, and Sentinel-1A and 1B) provide high resolution (100 m – 5 km) all-weather coverage; whereas passive microwave radiometers (Advanced SCATterometer (ASCAT) and AMSR-2) provide continuous spatial coverage at lower resolution (12.5 km – 25 km). Visible and infrared imagers (Moderate Resolution Imaging Spectroradiometer (MODIS) and Visible Infrared Imaging Radiometer Suite (VIIRS)) provide high resolution (250 m – 2 km) data but are generally light-dependent. Model output from the U.S. Naval Research Laboratory's Global Ocean Forecast System provides supplementary SIT and sea ice drift, and is used to determine atmospheric conditions that help in differentiating ice patterns. NIC analysts incorporate all of these available sea ice data sources, understanding the strengths and weaknesses of each, while generating their final sea ice charts – a result that is superior to any of the individual sources (C. Readinger, personal communication, July 27, 2022).

Sea ice charts from January 2003 onward are available to download from the NIC website (https://usicecenter.gov/Products/AntarcHome) in Environmental Systems Research Institute (ESRI) shapefile vector archival format. Charts from November 1997 through December 2002 are also available upon request in ESRI ArcInfo interchange (E00) format. Ice charts from 1972 to 1994 can be purchased on a CD-ROM from NOAA's National Centers for Environmental Information. Due to source data limitations, however, little information is provided beyond total SIC in the early charts

(before 1997). Charts were produced weekly from 1997-2002 and from 2014-2022 and biweekly from 2003-2013. In this study we use stage of development (S) and partial concentration (C) information included in NIC ice charts produced between November 1997 and December 2021.

2.3.6 SIT from NIC Charts

Shellenberg et al. (2003) introduced a method to estimate SIT in the Ross Sea during 1995-2000 based on NIC charts. It is calculated within polygons by summing the means of each thickness range multiplied by their corresponding partial concentrations. The resulting SIT dataset was compared to ship-based (ASPeCt) observations for preliminary validation. Deliberty et al. (2011) repeated this approach in the Ross Sea for 1995-1998 but included a more comprehensive set of ship-based SIT observations. To characterize SIV variability in the entire Southern Ocean, Morgan (2011) extended this method to 2000-2009. Orsi and Webb (2022) applied a modified version of this approach to the Sabrina Basin, East Antarctica and calculated the regional SIP.

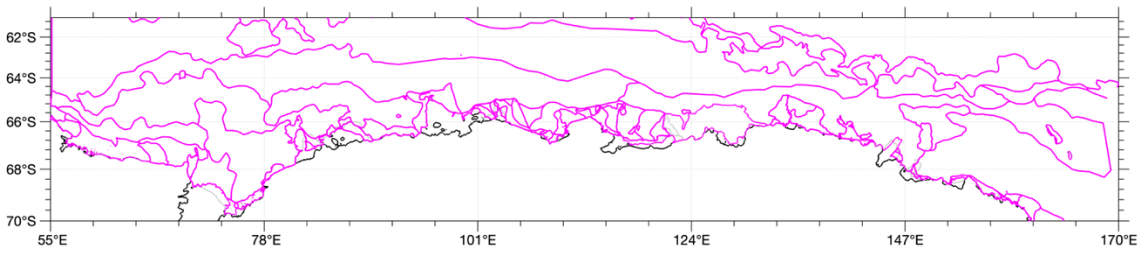

Figure 6. An example of the complexity of NIC ice chart polygons over the Antarctic continental margin.

Gridded fields provide the most readily useful format for multivariate data analyses. Over the shelf, NIC charts generally contain numerous relatively small polygons (Figure 6). In order to resolve these details we use the 3.125-km equal-area grid from the ASI SIC data. The entire Antarctic continental shelf is divided into eighteen working sectors inshore of the 1000-m isobath. These sectors were chosen to best characterize separate embayments found along the Antarctic coast. Farther offshore, where larger chart polygons are found, we use the 25-km equal-area grid from the SIM data. There is no overlap or significant gaps between sectors so that together they provide continuous and full coverage from the Antarctic coast to beyond the maximum winter sea ice edge.

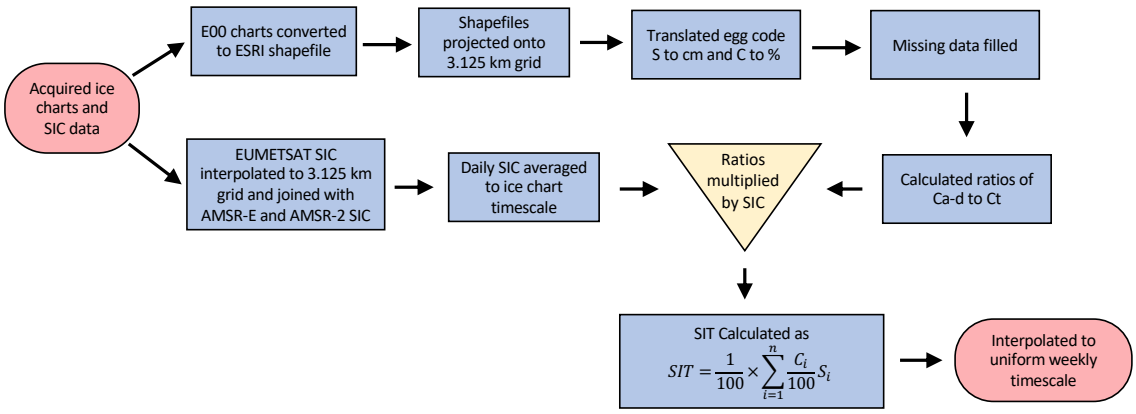

Figure 7. The process of converting ice charts and SIC data into weekly gridded SIT.

Significant processing of the source datasets is required to calculate SIT (Figure 7). Ice chart data produced between 1997 and 2002 in E00 format were first converted to ESRI shapefiles using GDAL, an open source library for geospatial conversions. Then

all shapefile data were projected to our working shelf (3.125 km) and oceanic (25 km) grids, by assigning at each grid point the value of the comprising polygon.

Table 1. SIGRID ice classifications, their thickness and concentration ranges, and the translated thicknesses and concentrations for each classification. Also listed are a few non-intuitive special conditions that must be known and addressed in order to correctly translate the egg code.

SIGRID S	Ice Type	Thickness Range	Translated T [cm]
55	Ice Free	-----	**0**
70	Brash Ice	<1 m - >4 m	-----
80	No Stage of Development	-----	**NaN**
81	New Ice	< 10 cm	**2.5**
82	Nilas, Ice Rind	< 10 cm	**5**
83	Young Ice	10 - <30 cm	**20**
84	Grey Ice	10 - <15 cm	**12.5**
85	Grey - White Ice	15 - <30 cm	**22.5**
86	First Year Ice	≥30 - 200 cm	**115**
87	Thin First Year Ice	30 - <70 cm	**50**
88	Thin First Year Ice Stage 1	30 - <50 cm	**40**
89	Thin First Year Ice Stage 2	50 - <70 cm	**60**
90	For Later Use	-----	**NaN**
91	Medium First Year Ice	70 - <120 cm	**95**
92	For Later Use	-----	**NaN**
93	Thick First Year Ice	≥120 cm	**150**
94	For Later Use	-----	**NaN**
95	Old Ice	-----	**265**
96	Second Year Ice	-----	**215**
97	Multi-Year Ice	-----	**300**
98	Glacier Ice	-----	**NaN**
99	Undetermined/Unknown	-----	**NaN**

Special Conditions
1. When a fourth ice type is present Cd = Ct-(Ca+Cb+Cc).
2. When only one ice type is present, partial concentration (Ca) shall not be specified. Thus Ca = Ct.
3. Any value intentionaly omitted is given a -9. Example: Sb, Sc, Ca, Cb, Cc when only one ice type is present.

SIGRID C	Concentration Range	Translated C [%]
55	Ice Free	**0**
01	< 1/10 (open water)	**5**
02	Bergy Water	**5**
10	1/10	**10**
12	1/10 - 2/10	**15**
13	1/10 - 3/10	**20**
20	2/10	**20**
23	2/10 - 3/10	**25**
24	2/10 - 4/10	**30**
30	3/10	**30**
34	3/10 - 4/10	**35**
35	3/10 - 5/10	**40**
40	4/10	**40**
45	4/10 - 5/10	**45**
46	4/10 - 6/10	**50**
50	5/10	**50**
56	5/10 - 6/10	**55**
57	5/10 - 7/10	**60**
60	6/10	**60**
67	6/10 - 7/10	**65**
68	6/10 - 8/10	**70**
70	7/10	**70**
78	7/10 - 8/10	**75**
79	7/10 - 9/10	**80**
80	8/10	**80**
81	8/10 - 10/10	**90**
89	8/10 - 9/10	**85**
90	9/10	**90**
91	9/10 - 10/10 or 9+/10	**95**
92	10/10	**100**
99	Undetermined/Unknown	**NaN**

Gridded Sa-d, Ca-d and Ct data were translated from the original SIGRID values to centimeters and percentages by assigning the mean of ranges associated with each sea ice category (Table 1). For example, gray ice (SIGRID S: 84) with a thickness range of 10-15 cm is assigned an average thickness of 12.5 cm. Similarly a SIGRID C: 56 indicating partial concentrations from 5/10 to 6/10 is assigned an average concentration

of 55%. This approach could lead to overestimation (underestimation) of SIT where ice of a certain S category is thinner (thicker) than the mean of its range. There are some intricacies in the SIGRID format and data availability that must be circumvented during translation. For example, when four ice types are defined but Cd is not provided, then it is calculated as the difference between Ct and the sum of Ca, Cb, and Cc. Also, often times only one ice type is defined and the missing value for Ca is assumed to be equal to Ct. Additionally, intentionally omitted data points flagged with a value of -9 must not be filled in, whereas the missing data points flagged with 99 are calculated (Appendix A). Finally, icebergs were traced in the NIC charts (SIGRID S: 98) but would periodically vanish for one or two weeks and needed to be replaced (Appendix A).

EUMETSAT SIC data (1978-2001) were linearly interpolated to ASI SIC (from 2002-present) data grid with 3.125-km spacing to extend the daily timeseries to 1978-2021. SIC data were then weekly/biweekly averaged from 1997 to 2021 to match NIC charts timescales. However, because of the coarser spatial resolution of Ct data included in the NIC chart polygons, and to preserve the same level of spatial detail available in the gridded SIC datasets, we replaced the single original Ct values within polygons with their corresponding finer gridded SIC distributions and calculated new ratio-based partial concentrations ($Cr_{a\text{-}d}$). In the end, area-averaged Ct data within polygons agree well with the original NIC chart single Ct values (Morgan, 2011), but they produce increased detail while estimating sea ice products such as SIT and SIV.

Sea ice thickness (H_g in m) is calculated at each grid point following DeLiberty et al. (2011):

$$H_g = \frac{1}{100} \times \sum_{i=1}^{n} \frac{Cr_i}{100} S_i$$

where n is the number of sea ice thickness categories (i; maximum of 4) defined at that grid cell and Cr_i and S_i are the category's ratio-based partial concentrations [%] and the stage of development [cm]. Finally we linearly interpolated the weekly/biweekly timeseries to uniform weekly.

Regional SIV [km^3] is calculated as:

$$SIV = \sum_{g=1}^{n} \frac{H_g}{1000} A_g$$

where n is the number of grid cells within the region and A_g is the area [km^2] of grid cell g.

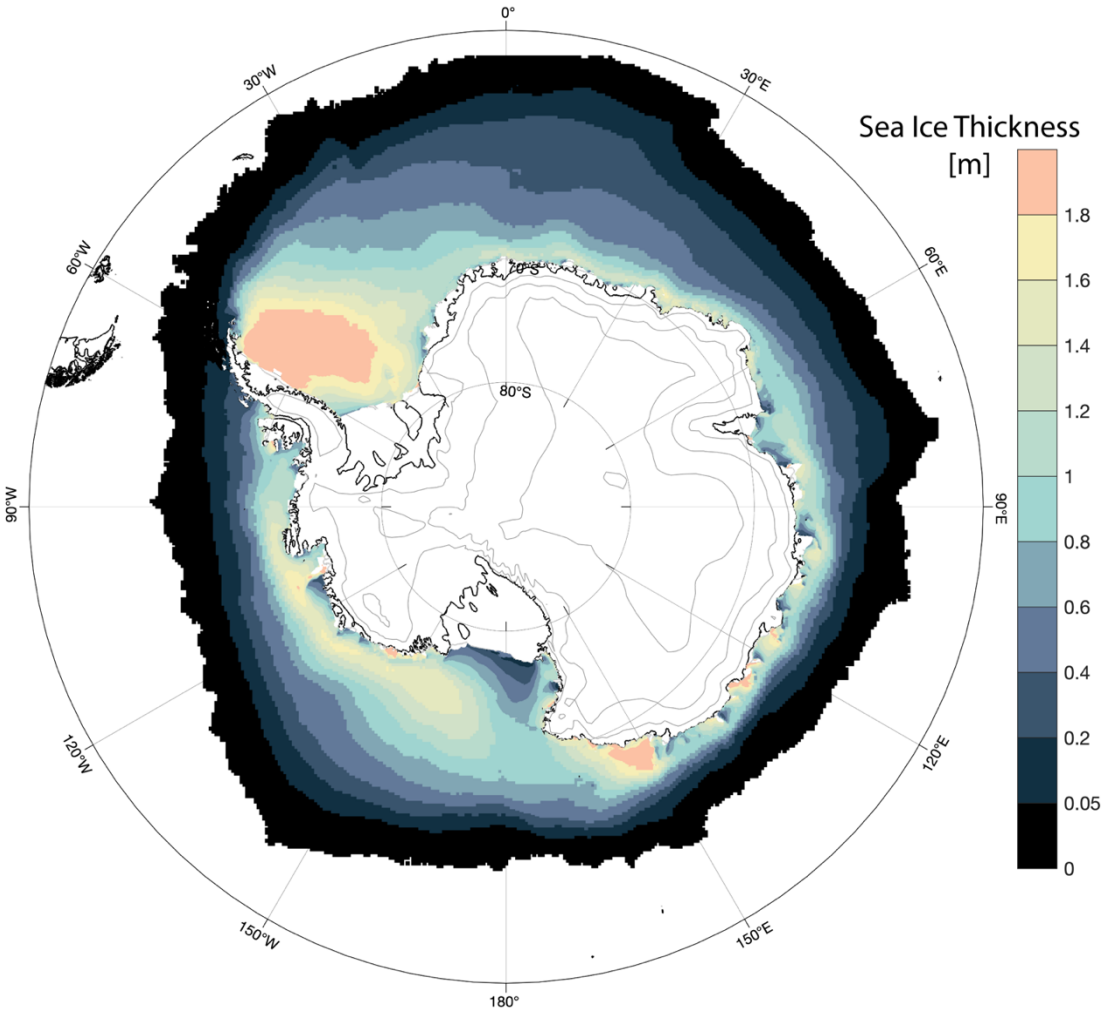

Figure 8. Mean SIT in the Southern Ocean during 1998-2021. The thickest ice is found just east of the Antarctic Peninsula and on the western sides of most East Antarctic embayments. Dark shades near the coast are places where polynyas likely form maintaining thinner mean sea ice than in the surrounding area.

The "empirical" S-based method described above results in a weekly high-resolution (3.125 km) SIT dataset (hereafter called SOD) that adequately portrays known areas with heavy ice, e.g. coastal western Weddell (SIT > 1.8 m) and offshore the Amundsen and Ross seas (1.2 m < SIT < 1.8 m), as well as with thin ice, e.g. numerous

coastal polynyas (SIT < 0.6 m near the coast) (Figure 8). Figure 8 also shows thick ice (SIT >1.8 m) on the western sides of embayments in the Indian sector. The Ross Sea Polynya starts to export newly formed sea ice as early as March, and shrinks until October (Figure. 9). The record-length monthly mean SIT for the Southern Ocean shows an apparent longer growth season, both in thickness and areal coverage from February/March to September/October, than melt season, by thinning and shrinkage from October/November to January/February. Throughout the year thick multiyear sea ice (SIT > 1.8 m) remains in the western Weddell Sea, but seasonal sea ice expands (shrinks) during the growing (melting) months.

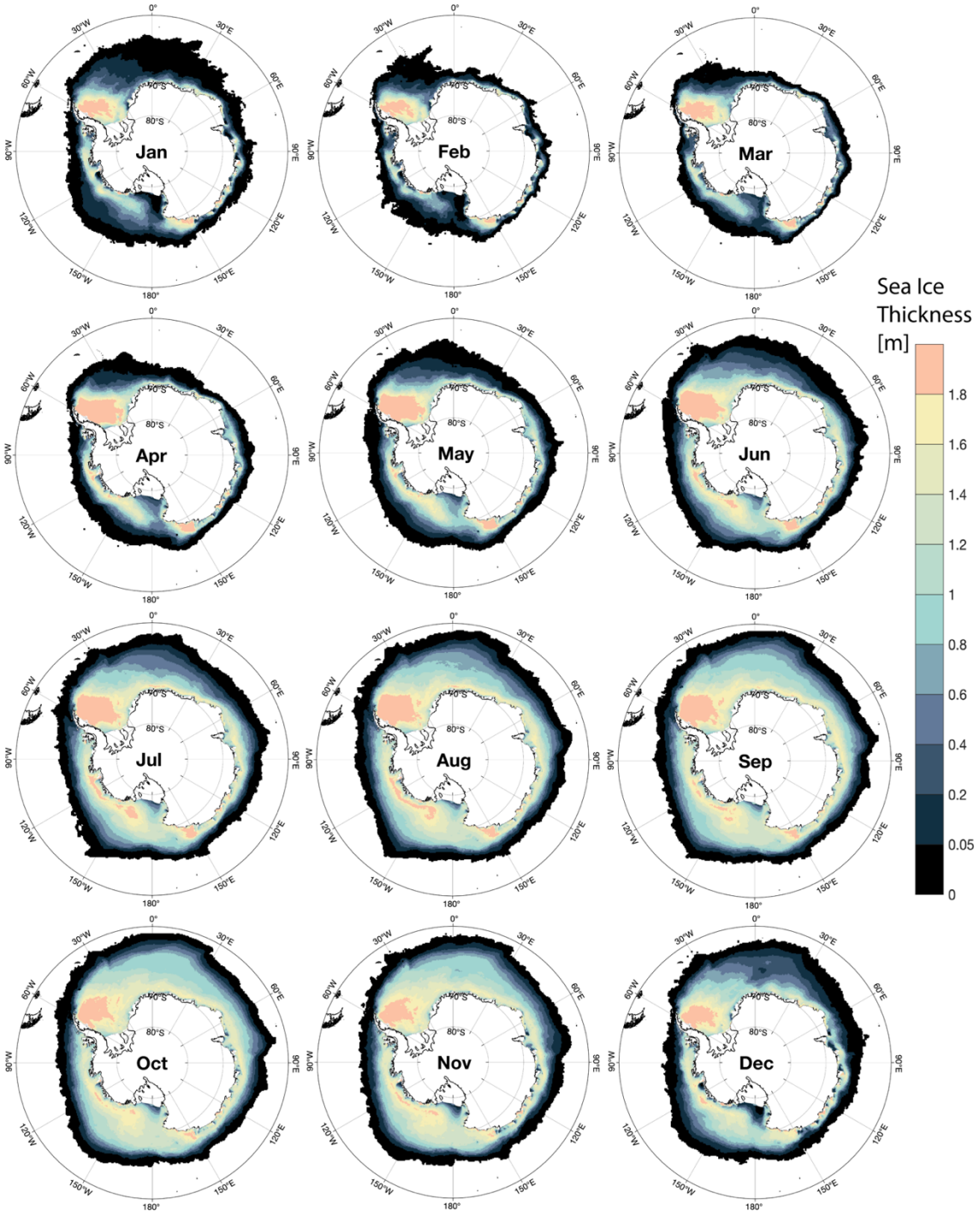

Figure 9. Monthly mean SIT in the Southern Ocean during 1998-2021. The typical asymmetrical cycle of slow growth (~7 months) and quick melt (~5 months) is apparent.

2.3.7 SIT Comparison

To compare all of the available SIT datasets generated with the methods described above (Table 2) SOD is first projected to matching spatial and temporal resolutions. To compare with ZIF and OLMi, SOD data are interpolated along the satellite tracks and averaged over the ~34 day campaign periods. To compare with ESCS and GIOMAS, SOD data are calculated as monthly averages and interpolated to their grids (50 km and 0.8º). Because the ESCS SIT data only represent whatever type of sea ice is found within a given grid point area regardless of the relative abundance – e.g. if 80% of a grid cell area is open water and the remaining 20% has 3 m thick multiyear ice the ESCS SIT value assigned to that grid cell would be 3 m – it is here multiplied by the matching SIC data. ESCS and GIOMAS datasets have global coverage and are thus available for comparison of total SIV; whereas ZIF and OLMi (satellite track-following) datasets are only suitable to compare mean SIT.

Table 2. Spatial resolution, temporal coverage, and data sources for the SIT approaches discussed here. SOD is the SIT dataset produced during this study.

Method	Resolution	Temporal Coverage	Source
ZIF	ICESat Tracks	2003-2008	ICESat
OLMi	ICESat Tracks	2003-2008, 2018-2019	ICESat, ICESat-2
ESCS	50 km	2002-2016	Envisat, Cryosat
GIOMAS	0.8 degree	1978-present	Model
SOD	3.125 km shelf 25 km offshore	1998-present	NIC Charts

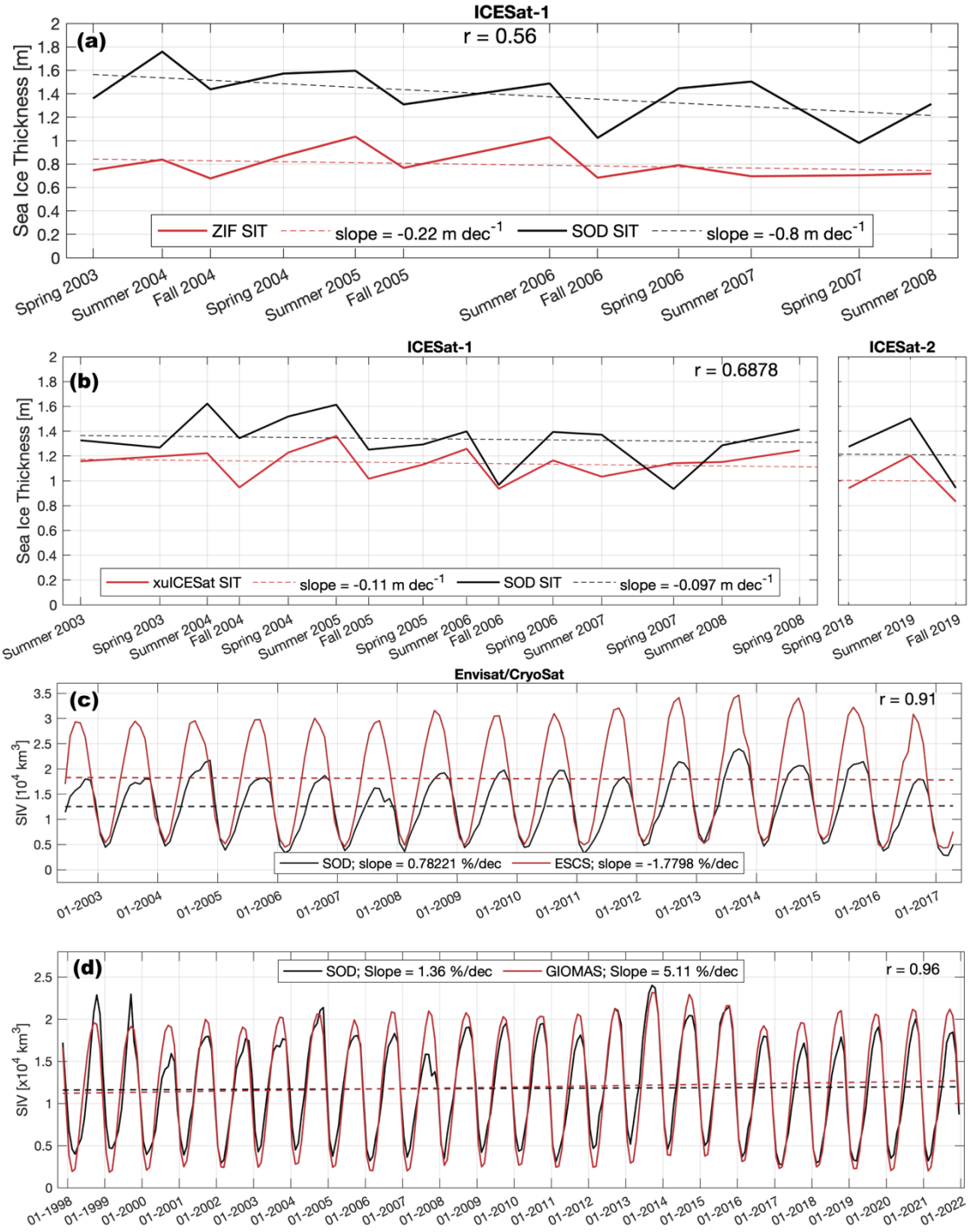

Figure 10. Comparisons of SOD SIT with: (a) Kurtz and Markus (2012) ZIF, (b) Xu et al. (2021) OLMi, (c) Hendricks and Rinne (2018a) and (2018b) ESCS, and (d) GIOMAS model output including linear best fit lines, their trends, and correlation coefficients (r). In (a) and (b) we compare mean SIT along satellite tracks and in (c) and (d) we compare Southern Ocean SIV.

Figure 10a shows that the ZIF approach delivers a mean SIT (0.8 m) that is considerably thinner than the 1.4 m from SOD. Correlation between these two time series is moderate ($r = 0.56$) and SOD's thinning of -0.8 m/decade is considerably faster than ZIF's of -0.22 m/decade. OLMi (Figure. 10b) renders a mean SIT of 1.12 m, i.e. higher than ZIF's but closer to SOD's 1.32 m. The OLMi time series also shows roughly the same thinning trend as the SOD's, of about -0.1 m/decade and with relatively higher correlation ($r = 0.69$). The disagreement between SOD and both the ZIF and OLMi datasets is greater in the summer (Figure 10a-b), when thin (SIT < 1 m) ice types and heavy snow loading are less prevalent and the ZIF/OLMi data are more error prone.

ESCS SIV agrees well with SOD during summer (December/January to February/March) but it also shows values about twice as high during winter (Figure 10c). Although both time series have similar annual cycles and are highly correlated ($r = 0.91$), SOD's growth trend of 0.78 %/decade disagrees both in magnitude and sign with ESCS's decay of -1.78 %/decade. The large winter differences are likely the result of more snow loading leading to ESCS overestimation, as explained above.

Over a longer record, GIOMAS SIV closely matches SOD values throughout the year ($r = 0.96$), but it also consistently overestimates winter and summer extremes (Figure 10d). Also, GIOMAS SIV shows a significantly faster growth rate (5.11 %/decade) than SOD (1.36 %/decade). While rendering similar total SIV means (GIOMAS of 1.19×10^4 km^3 and SOD of 1.18×10^4 km^3), there are some geographical differences worth noting. GIOMAS shows thinner sea ice in the central Weddell Sea and near the East Antarctic continental margin, and thicker sea ice farther offshore and

within coastal polynyas (Figure 11). Specifically, SOD shows more sea ice in the 1.7-2.7 m thickness range, while GIOMAS shows more in the 0.7-1.6 m thickness range (Figure 12).

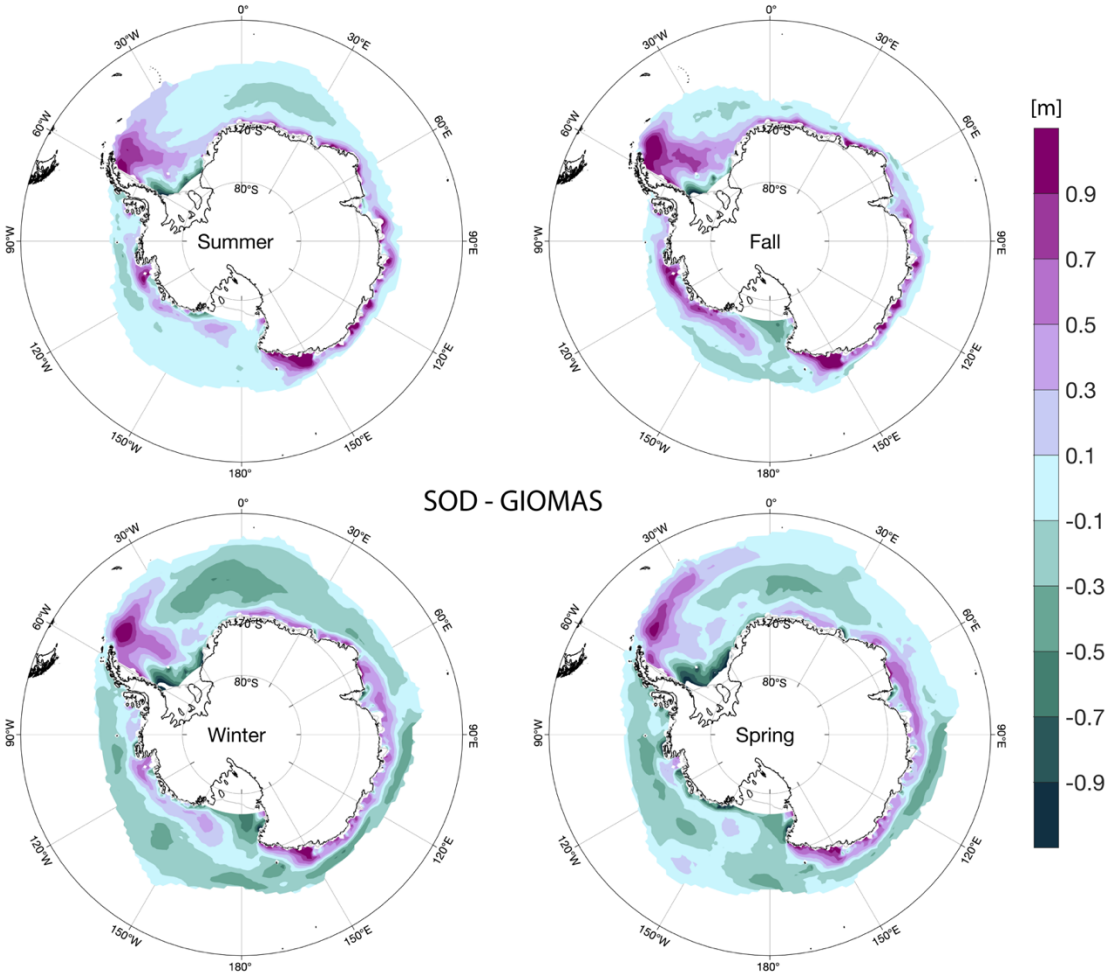

Figure 11. Seasonal differences between SOD and GIOMAS SIT. In purple (green) areas SOD (GIOMAS) shows thicker ice.

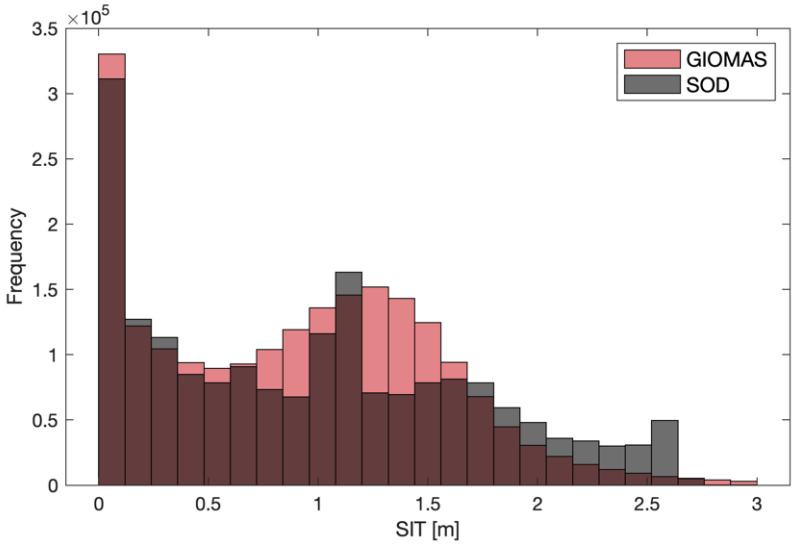

Figure 12. Distribution of SIT in the GIOMAS and SOD datasets. GIOMAS shows more ice in the 0.7-1.6 m range while SOD shows more in the 1.7-2.6 m range.

CHAPTER III

CALCULATING SIP

Estimating SIP at different sectors of the Antarctic continental shelf assumes that it is proportional to the net SIV transport (SIVT) through their outer gate and to the net SIV change within the region's interior. We defined all transport gates as a series of points 25 km apart from each other (Figure 13) and located inshore of the 1000-m isobath. They are intended to enclose distinct shelf segments based on the most salient features of the coastline, local bathymetry and sea ice, glaciers and ice shelves. In several areas around East Antarctica the gate ends are located at protruding ice tongues. Gate coastal proximity was mainly dictated by the available SIM data with 25-km grid spacing. Segments where the shelf is particularly narrow and there is no adequate SIM data are not included in this analysis; but their relatively small areas and lack of large polynyas suggest minimal SIP.

SIVT is calculated using weekly SIT and SIM data interpolated to the gate points 25 km apart. Average SIT and SIM are calculated at gate midpoints, and the SIM component perpendicular to the gate (nSIM) is used (Figure 14) to compute SIVT [km^3/week] as:

$$SIVT = \sum_{i=1}^{n} SIT_i \times nSIM_i \times L$$

where n is the number of midpoints along the gate and L is 25 km. Positive (negative) SIVT corresponds to sea ice leaving (entering) the "gated" sector. For a given shelf sector and week, the net SIVT across the entire length of the gate may result in either a regional export or import of SIV.

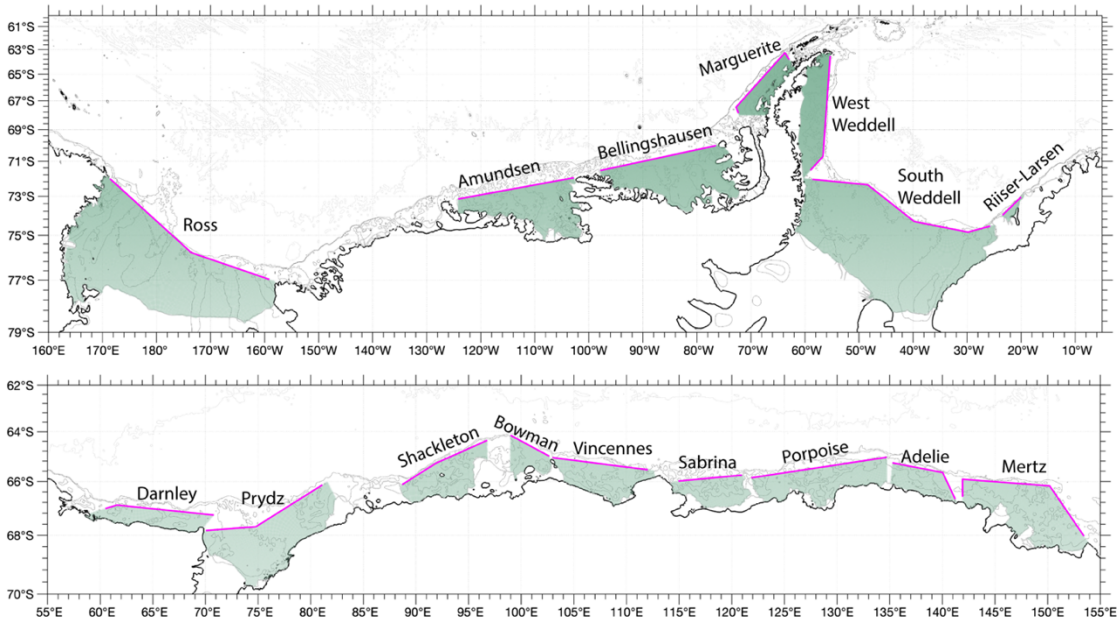

Figure 13. All sectors in which SIP calculated and their gates. Flux gates end at protruding permanent ice features or as near the coast as the SIM data domain allows.

Regional SIP (Table 3) was then calculated by summing change in interior SIV (ΔSIV) [km^3/week] and net SIVT [km^3/week]. The primary contributor to regional SIP is SIVT (export). ΔSIV only slightly enhances summer/fall SIP with interior growth (expansion), and reduces winter/spring SIP with interior decay (Figure 15).

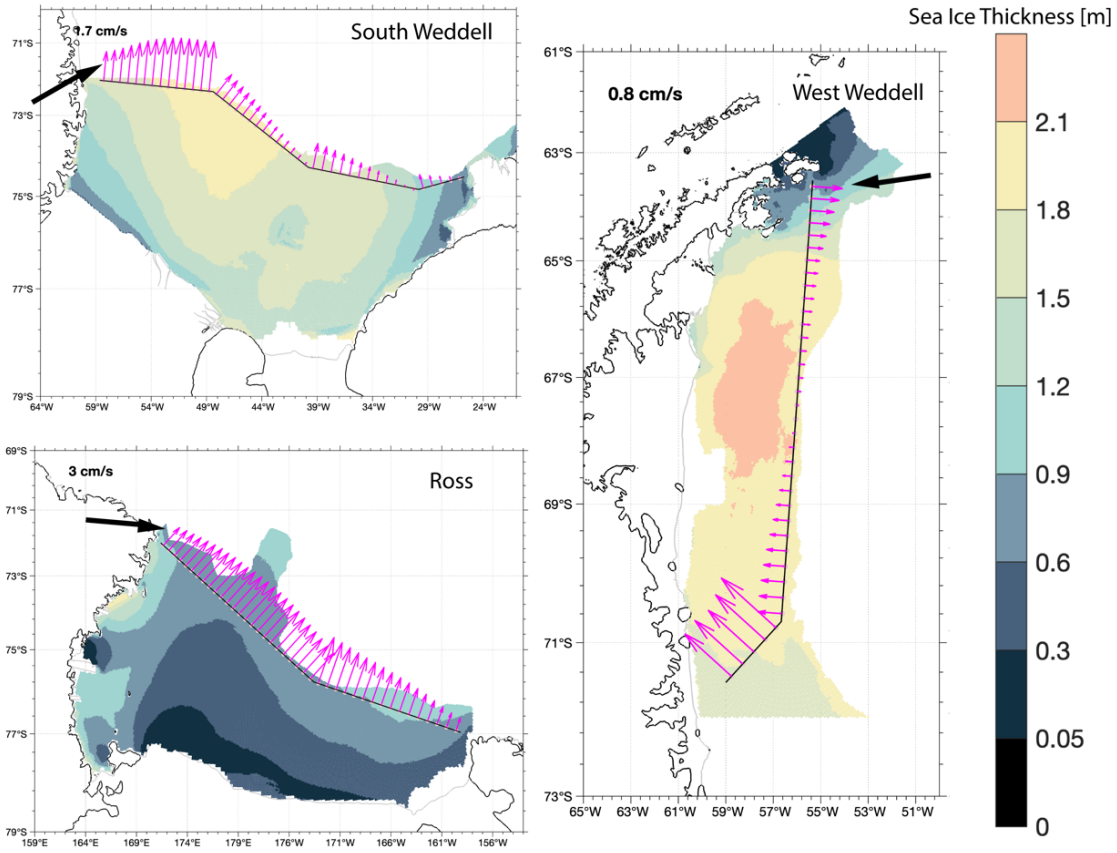

Figure 14. Mean SIM normal to the gate and SIT at three example regions: Southern Weddell and Ross are the two most productive while West Weddell is the most negative. The speed of the first vector (signified with black arrow) is listed at the top left of each plot for scale.

Table 3. Mean yearly SIP, Transport, Change in interior SIV, Productivity (SIP/area), and SIP trends.

Sector	Mean Yearly SIP km^3	Mean Yearly Transport [km^3]	Mean Yearly ΔSIV [km^3]	Productivity [m]	SIP Trend [%/Dec]
Ross	1010	1016.88	-6.89	2.98	-30
Southern Weddell	799.46	791.05	8.41	2.15	2.4
Prydz	267.14	266.75	0.39	3.44	-7.1
Bellingshausen	218.57	218.91	-0.34	1.3	-47.6
Amundsen	182.89	187.19	-4.3	1.7	-33.3
Mertz	128.46	129.6	-1.13	1.7	-40.3
Darnley	91.64	91.93	-0.28	3.06	-2.3
Shackleton	72.05	73.15	-1.1	1.5	-44.1
Riiser-Larsen	66.17	66.14	0.03	14.86	-19.4
Sabrina	55.04	55.47	-0.43	1.94	-50.1
Vincennes	53.24	54.67	-1.43	1.31	-87.4
Porpoise	30.92	33.15	-2.23	0.55	-133.8
Adelie	-7.83	-7.25	-0.59	-0.34	270
Bowman	-20.97	-20.4	-0.58	-1.03	71.7
Marguerite	-27.8	-27.63	-0.16	-0.34	24.8
West Weddell	-70.48	-64.38	-6.09	-0.51	-9.4
Totals	2848.5	2865.23	-16.72		

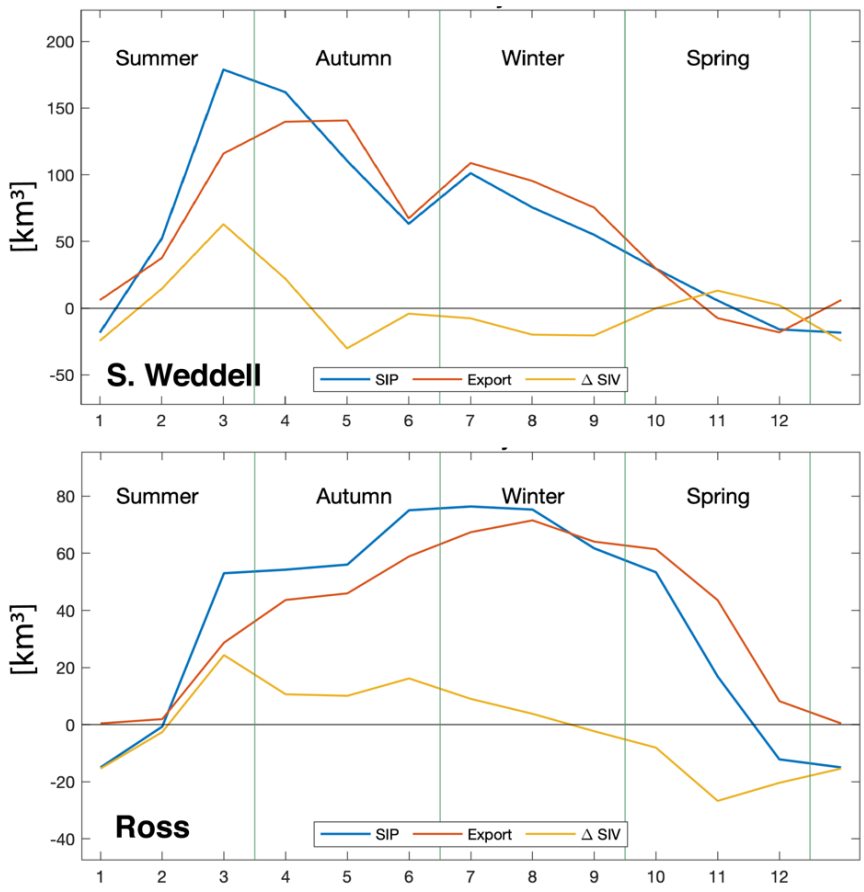

Figure 15. Climatological annual cycles of SIP, Net export (transport), and change in interior SIV in the South Weddell and Ross regions. ΔSIV does not significantly impact total SIP but does intensify growing and melting periods.

CHAPTER IV

RESULTS

The sensitivity of SIP estimates to the choice of SIT fields, either empirical SOD or modelled GIOMAS, is estimated next. Then, regional SOD SIP rates are compared to those reported by Tamura et al. (2016) using the "thin ice thickness" approach.

4.1 SIP rates from GIOMAS SIT

Relatively coarse resolution (0.8 º) GIOMAS SIT data are interpolated to the outer gate points (25 km apart) and interior grid points (3.125 km spacing). There are some minor voids in the GIOMAS SIT data close to glaciers and ice shelves that prevent interpolation to the full interior grid, thus only small ΔSIV values are likely missed with minimal influence on regional SIP estimates. SOD SIP is also compared to GIOMAS SIP at its original SIT monthly intervals.

The total annual mean GIOMAS SIP rate for all the shelf sectors is 3033.02 km^3/year, somewhat (6.5%) higher than the 2848.5 km^3/year estimated from SOD SIP (Table 4). There are significant regional differences, however: GIOMAS SIP renders much higher rates in the Weddell (22.4%) and Bellingshausen (43%) seas, and slightly lower rates over much of the Indian sector. Additional difference are apparent in the timing of the yearly cycle: SOD generally shows increasing and decreasing SIP rates earlier than GIOMAS (Figure 16). A third source (satellite) of gate SIT from ESCS is used to investigate how it affects the SIP timing.

Table 4. SOD SIP and GIOMAS SIP and their trends. The last three columns show the correlation coefficients for SOD, GIOMAS, and ESCS SIT along the flux gates with interior SIC.

	Yearly SIP [km^3]		SIP DIFFERENCE	Yearly SIP Trends [%/dec]		r between gate SIT and interior SIC		
Sector	SOD	GIOMAS	SOD-GIOMAS	SOD	GIOMAS	SOD	GIOMAS	ESCS
Ross	1010	1022.9	-12.9	-30	-10.5	0.68	0.9	0.68
Southern Weddell	799.46	978.86	-179.4	2.4	9.7	0.49	0.61	0.37
Prydz	267.14	179.31	87.83	-7.1	-24.1	0.69	0.87	0.71
Bellingshausen	218.57	312.57	-94	-47.6	4	0.73	0.83	0.7
Amundsen	182.89	182.23	0.66	-33.3	-25.5	0.68	0.69	0.67
Mertz	128.46	110.09	18.37	-40.3	-29.6	0.75	0.83	0.59
Darnley	91.64	41.52	50.12	-2.3	-31.1	0.59	0.81	0.57
Shackleton	72.05	48.23	23.82	-44.1	-3.7	0.59	0.81	0.6
Riiser-Larsen	66.17	69.12	-2.95	-19.4	21.4	0.58	0.74	0.62
Sabrina	55.04	45.67	9.37	-50.2	-45.3	0.52	0.71	0.54
Vincennes	53.24	46.42	6.82	-87.4	-62.7	0.65	0.77	0.58
Porpoise	30.92	38.93	-8.01	-133.9	-85.6	0.67	0.79	0.56
Adelie	-7.83	13.28	-21.11	270.2	-120.8	0.65	0.86	0.55
Bowman	-20.97	-2.81	-18.16	71.8	173.9	0.54	0.75	0.48
Marguerite	-27.8	-14.07	-13.73	24.8	51.1	0.76	0.84	0.62
West Weddell	-70.48	-39.23	-31.25	-9.4	-24	0.6	0.71	0.6
totals/means	2848.5	3033.02	-184.52			0.64	0.78	0.59

Figure 16. Climatological annual cycles of SIP from SOD and GIOMAS SIT.

The overall mean SIT along the outer gates is similar in most of the regions, but the timing of thickening and thinning differed (Figure 17) leading to contrasting yearly SIP cycles. In some sectors (Figure. 17c) the ESCS timing is similar to SOD, in spite of showing a considerably higher peak in April; while in other regions (Figure 17a) it agrees more with GIOMAS increasing from March to August-September. In the Ross (Figure 17d), SOD and GIOMAS annual cycles agree (maximum in September, minimum in February) but both extremes occur a month earlier in the ESCS.

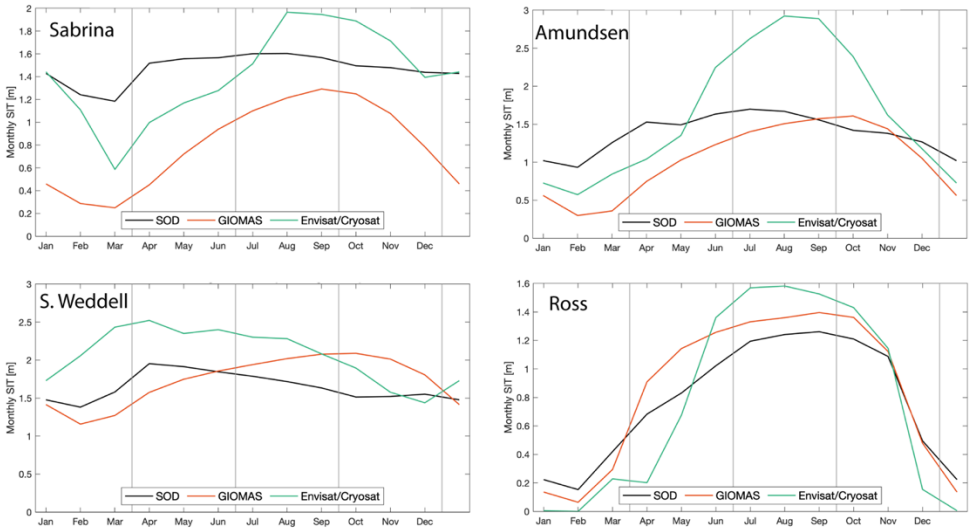

Figure 17. Climatological annual cycles of SIT from SOD, GIOMAS, and ESCS along the flux gates. Vertical gray lines represent seasonal divisions starting with summer (December 16 to march 15).

4.2 Thin Ice Thickness SIP

The "thin ice thickness" approach to estimate SIP is limited to coastal polynyas where the ice is less than 0.2 m thick. To compare SOD SIP rates to those reported by Tamura et al. (2016) a series of new gates are defined farther inshore to more closely

bound the coastal polynyas. Where multiple polynyas are found within the same shelf embayment, e.g. in the Prydz Bay and the Ross Sea, their reported SIP values are combined. Likewise, in areas like the Weddell Sea where their polynya extends through this study's West and Southern Weddell sectors, the latter regional SIP values are combined. This study reports significantly higher SIP rates than Tamura et al. (2016) over the largest embayments: 130.6% in the Ross and 193.4% in the Weddell; but lower over smaller Indian and Eastern Pacific regions: 50.5% in Darnley, 25% in Mertz, 41.5% in Shackleton, 41.1% in Vincennes, and 61.3% in Dibble (Table 5). Overall, the total annual mean SIP rate from this study is 1,136 km^3/year higher (63.9%) than that reported by Tamura et al. (2016). SIP rates estimated using "polynya" gates result in a total of 1,762 km^3/year, i.e. only 17 km^3/year lower than Tamura et al. (2016), but still show some important regional differences (Table 5).

Table 5. SIP from Tamura et al. (2016) and from this empirical approach

Polynya	Sector	Tamura 2016 Mean Yearly SIP [km^3]	Whole Sector Mean Yearly SIP [km^3]	Whole sector Difference (SOD-Tamura)	Polynya Only Mean Yearly SIP [km^3]	Polynya Only Difference (SOD-Tamura)
Ross + Terra Nova	Ross	438	1010	572	494	56
Weddell	South + West Weddell	271	795	524	487	216
Darnley	Darnley	182	90	-92	65	-117
Mertz	Mertz	172	129	-43	129	-43
Amundsen	Amundsen	123	183	60	87	-36
Shackleton	Shackleton	123	72	-51	80	-43
Barrier + Mackenzie	Prydz	190	278	88	170	-20
Vincennes	Vincennes	90	53	-37	78	-12
Dibble	Porpoise	80	31	-49	25	-55
Bellingshausen	Bellingshausen	59	219	160	57	-2
Dalton	Sabrina	51	55	4	90	39
	Total	1779	2915	1136	1762	-17

SOD's SIP in the South and West Weddell sectors combined is 795 km^3/year and consistent to commonly observed narrow coastal polynyas; whereas the “thin ice” approach struggled to capture them and rendered only 271 km^3/year (Tamura et al., 2016). Similar disagreements are indicated in the Bellingshausen Sea, where the SOD SIP exceeds the "thin-ice" estimate by 160 km^3/year, in the Prydz Bay by 88 km^3/year, in the Amundsen Sea by 60 km^3/year, and in the Ross Sea by 56 km^3/year. In five other sectors, however, the reported SIP rates from the "thin-ice" method are higher than SOD's, with differences ranging from 37 to 92 km^3/year. Note also that the timeframe (1992-2015) in Tamura et al. (2016) is earlier than for this study (1998-2020), which could lead to lower SIP rates if one considers the reported positive SIV trends.

4.3 Regional SIP

The large coastal polynyas found in broad continental shelves produce the most volumes of sea ice. The Ross Sea stands out with the highest estimated SIP around Antarctica, an average 1,010 km^3/year, followed by the southern Weddell Sea with 800 km^3/year. Together they produce 63.6% of the total mean annual SIP. Mid-range SIP rates are estimated in the Prydz (267 km^3/year), the Bellingshausen (219 km^3/year), and the Amundsen (183 km^3/year). These three regions account for 23.5% of total mean annual SIP. Multiple lower-range SIP sectors are located over East Antarctica: Mertz (128 km^3/year), Darnley (92 km^3/year), Shackleton (72 km^3/year), Riiser-Larsen (66 km^3/year), Sabrina (55 km^3/year), Vincennes (53 km^3/year), and Porpoise (31 km^3/year). The combined SIP from all seven sectors accounts for only 17.5% of total mean annual

SIP. Four sectors have net annual losses of SIV and their estimated annual SIP rates are negative, even though all of them actually produce some SIV during the fall and winter (Figure 18): West Weddell (-70 km^3/year), Marguerite (-28 km^3/year), Bowman (-21 km^3/year), and Adelie (-8 km^3/year) sectors. However, all together they reduce the total mean annual SIP by only 5.5%.

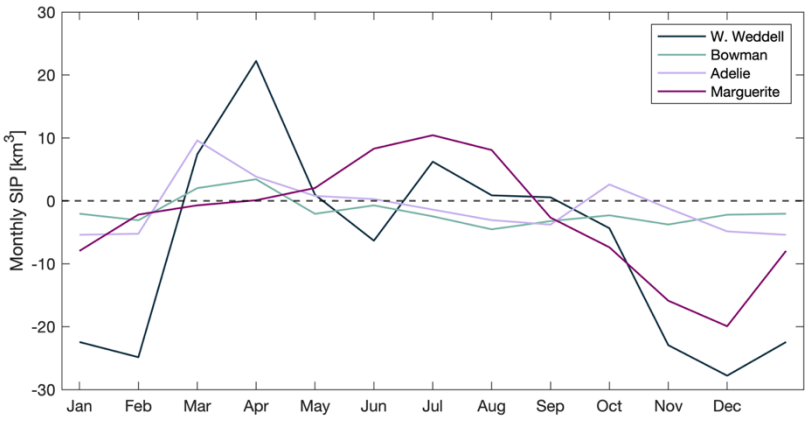

Figure 18. Climatological annual cycles of SIP in the regions where sea ice generally melts (SIP < 0). Though these regions are net sinks of sea ice, they still produce ice during at least part of the year. West Weddell, Bowman, and Adelie produce early in the season but quickly cease while Marguerite's cycle is more typical of productive sectors and SIP continues until near the end of winter.

Many of the lower-range SIP sectors are also small in areal extent. Therefore, when considering sector productivity [m/year], i.e. the sector's SIP per unit area, the Riiser-Larsen shows the highest rate (14.9 m/year) even though it has the smallest gated area and relatively little total SIP. Sectors with the next highest estimated SIP are Prydz (3.44 m/year), Darnley (3.06 m/year), and Ross (2.98 m/year) (Table 3).

Negative 1998-2020 trends in SIP are indicated almost everywhere around the continent. The strongest reductions in SIP are apparent in the Porpoise (-13.4%/year) and Shackleton (-8.7%/year) sectors, whereas lower loss rates are estimated in the Ross Sea (-3%/year). In contrast, the Weddell Sea shows a slight increase in SIP (0.2%/year). The long-term regional changes in SIP rates reported above ought to be apparent in the salinity records of surface waters. This in turn might elucidate if a particular shelf sector is likely to gain, retain, or lose its current ability to produce dense SW and AABW, i.e. change its role in the global MOC.

4.4 Upper Water Salinity

AASW properties in the top ~100 m of the Antarctic continental shelf show relatively large seasonal variability. However, intense winter cooling and sea ice formation result in a thick homogeneous surface layer with near freezing temperature. Since the vast majority of all available measurements are from the summer, the evolution of the Winter Thermostad Water (WTW) characteristics remains undersampled. Its summer subsurface remnant is apparent as a temperature minimum (often called Winter Water). Continuous salt released during sea ice formation increases WTW salinity, and decreases its buoyancy above local varieties of Thermocline Water. At some shelf locations this process is intense enough for the WTW salinity to exceed the critical value of 34.52, producing new SW volumes with a range of salinities (densities) that become unstable and sink to deeper equilibrium levels. The evolution of regional (within gated sectors) WTW salinity are calculated using the SIP rates

estimated in this study, to assess their impact on the variability of AASW and SW characteristics. The initial summer expression of WTW salinities in each sector are determined from inspection of the comprehensive WOCE Southern Ocean DataBase available to this study. When sufficient SIP increases the WTW salinity past 34.52 the additional salt is exported to the deeper layer. The WTW salinity also reflects the freshening influence of the most prominent and well-documented meltwater inputs from multiple ice shelves and glaciers (Rignot et al., 2013). We also investigate the hypothetical glacial melt rates required to intermittently disrupt convection in the Ross and Weddell regions.

Weekly changes in the regional WTW salinity (ΔS) represent the net result of adding salt and freshwater from sea ice production and meltwater injection. It is assumed that on average 79% of the salt contained in freezing seawater is released to the WTW layer (Skogseth et al., 2004). At each weekly interval the WTW salinity is calculated as:

$$S = \begin{cases} \left(m_{salt} + \left(m_{sf} \times 0.79\right)\right) / \left(m_{sw} + m_{sf} \times 0.79 + m_g - m_{fwf}\right), & SIP > 0 \\ \left(m_{salt} + \left(m_{sf} \times 0.21\right)\right) / \left(m_{sw} + m_{sf} \times 0.21 + m_g + m_{sim}\right), & SIP < 0 \\ m_{salt} / \left(m_{sw} + m_g\right), & SIP = 0 \end{cases}$$

Where m_{salt} (m_{sw}) is the mass of salt (seawater) in the upper 400 meters of seawater, m_{sf} is the mass of salt released by the volume of seawater that froze according to the estimated regional SIP rate (with SIV produced or melted), m_g is an estimated mass of

regional glacial meltwater input, m_{sim} is the mass of freshwater added during melting of sea ice, $and\ m_{fwf}$ is the mass of freshwater lost during sea ice formation.

In the Ross Sea, high SIP rate and local meltwater input (91.5 Gt/year) result in winter convective periods of ~200 days each year (Figure 19a). Including the additional import of 518 Gt/year of meltwater derived potentially from the Amundsen Sea, i.e. primarily from the Pine Island, Thwaites, Dotson, and Getz glaciers, the duration of convective periods in the Ross Sea is reduced to ~100 days and decreasing further since 2003 (Figure 19b). Only a hypothetical total (local plus imported) meltwater input of 700 Gt/year is sufficient to intermittently halt convection in the Ross Sea (Figure 19c), and there would be no local SW formation since 2014.

In the southern Weddell Sea, the high regional SIP rate dominates the influence from local (159 Gt/year) and imported (241 Gt/year) meltwater inputs to result in a more convection-prone WTW (Figure 20b) during winter periods about 150 days long. An hypothetical meltwater input of 500 Gt/year would intermittently halt convection in the southern Weddell Sea (Figure 20c) but only until 2015. Prydz Bay consistently produces SW during the winter, in spite of the local meltwater input of 64.2 Gt/year (Figure 21a), and as much as a 170 Gt/year input would be needed to intermittently halt local convection (Figure 21b).

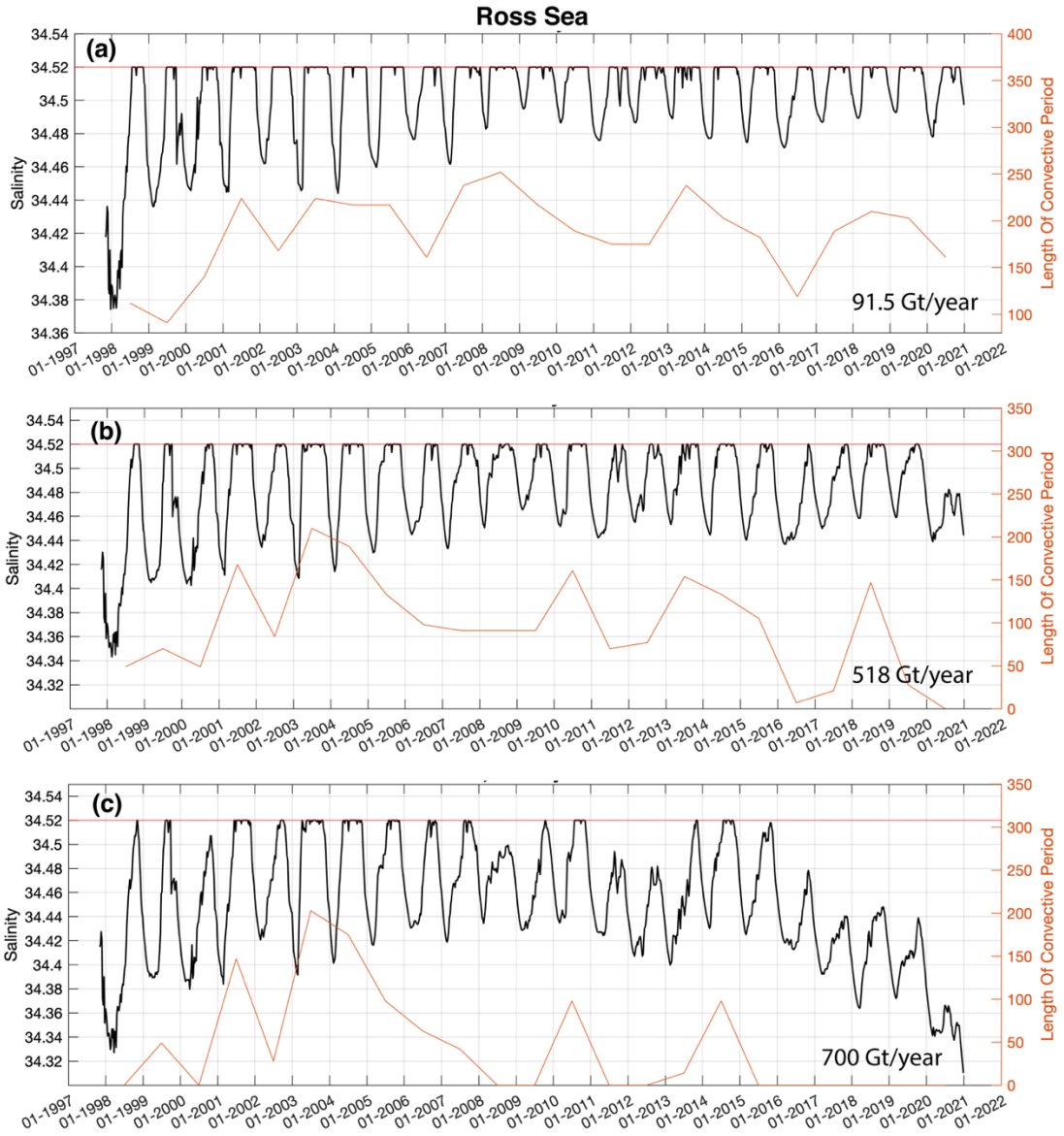

Figure 19. Salinity timeseries in the Ross Sea with (a) only local meltwater, (b) local melt plus meltwater from upstream including Getz Glacier and those in the Amundsen Sea, and (c) a theoretical melt rate of 700 Gt/year which is sufficient to intermittently halt convection.

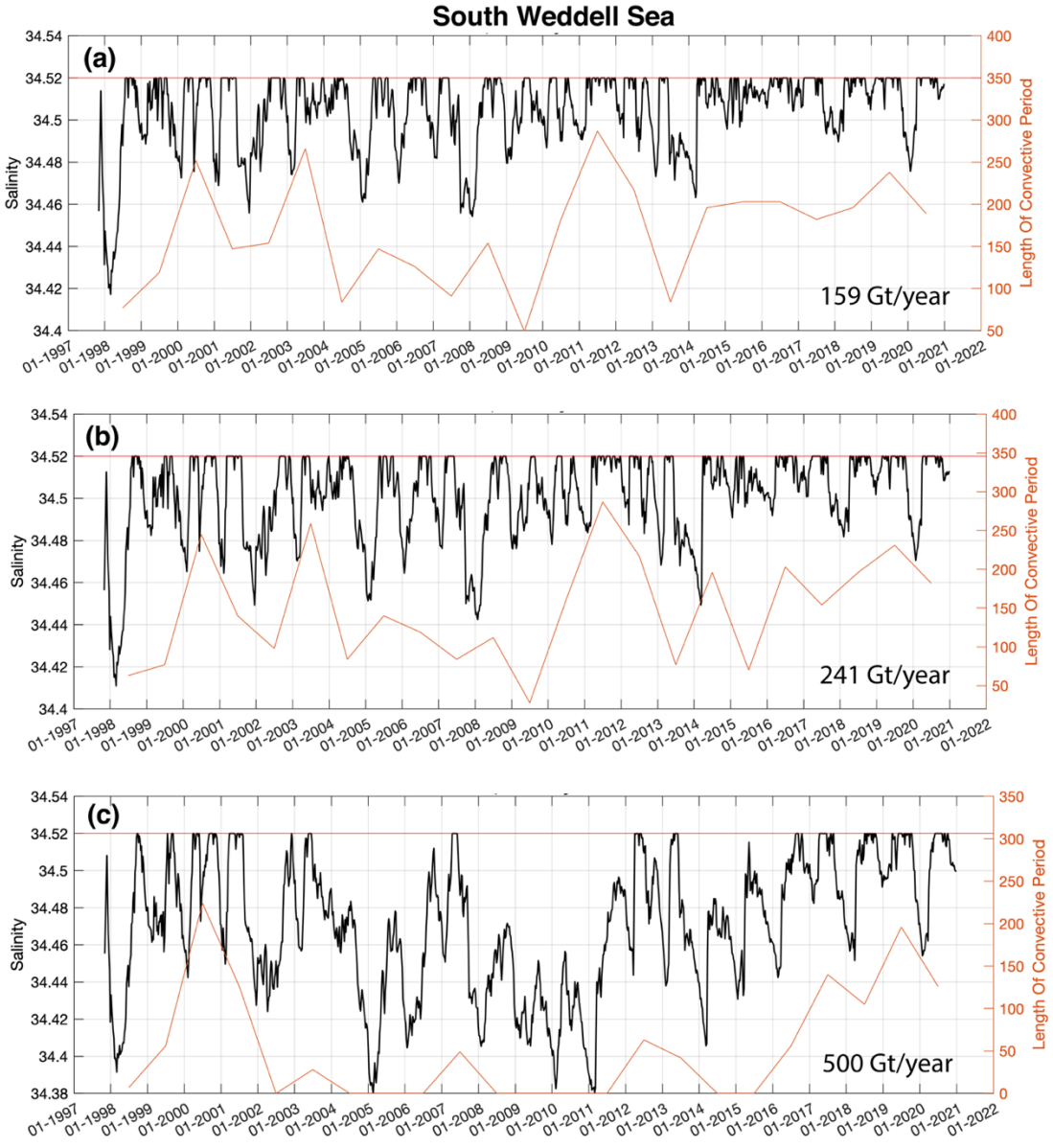

Figure 20. Salinity timeseries in the South Weddell Sea with (a) only local meltwater, (b) local melt plus meltwater from upstream including all glaciers between the South Weddell sector and Prydz Bay, and (c) a theoretical melt rate of 500 Gt/year which is sufficient to intermittently halt convection.

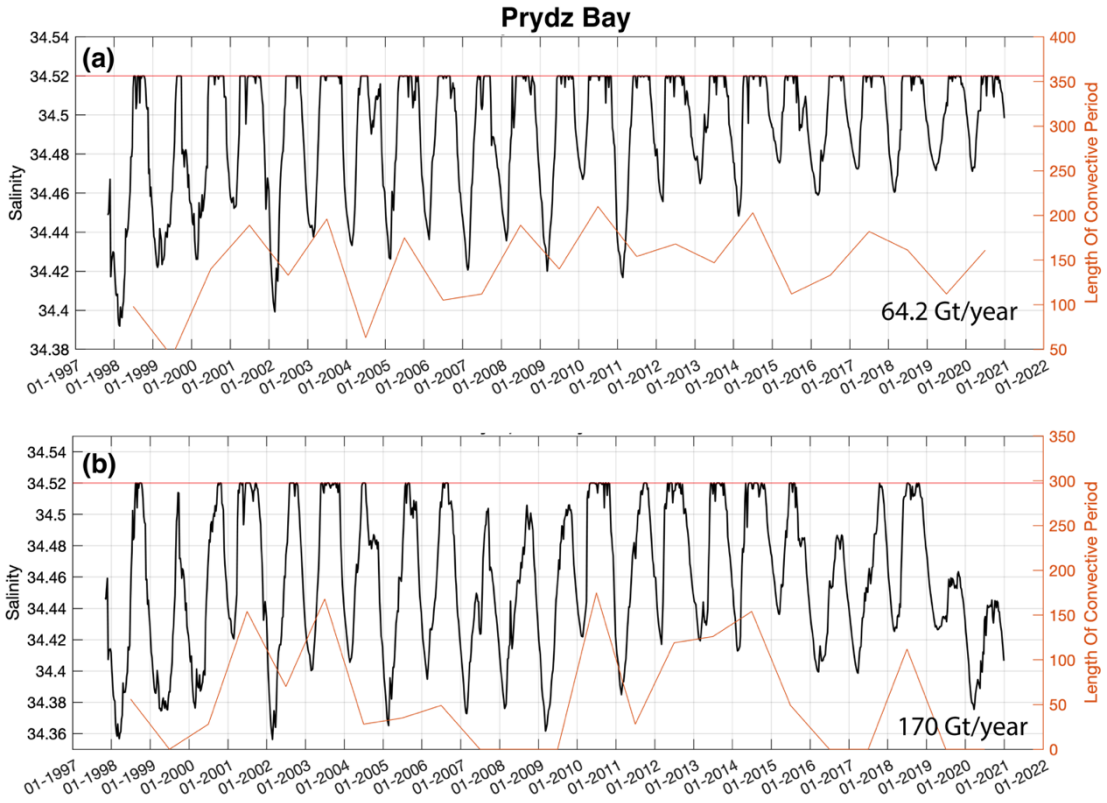

Figure 21. Salinity timeseries in Prydz Bay with (a) local meltwater and (b) a theoretical melt rate of 170 Gt/year which is sufficient to intermittently halt convection.

CHAPTER V

CONCLUSIONS

Sea ice formation over the Antarctic margins controls the intensity of near-boundary convection and influences the lower limb of the global Meridional Overturning Circulation. While at the present time estimating Sea Ice Thickness is challenging, it is a crucial step toward better understanding interannual to decadal variability in Antarctic Sea Ice Volume. Current altimetry-based methods to determine Sea Ice Thickness are biased due to large uncertainty in snow load coverage and thickness. Modelled (GIOMAS) Sea Ice Thickness fields recreate temporal variability fairly well, but they struggle to reproduce polynyas and prominent thick ice regions and the current spatial and temporal resolutions of many are still inadequate to fully resolve sea ice characteristics over the Antarctic continental shelf. The empirical approach followed in this study relies heavily on analyst-produced NIC ice charts, and generates more realistic Sea Ice Thickness fields than those derived entirely from remote sensing or thermodynamical models. The new NIC chart-based Sea Ice Thickness dataset, together with Sea Ice Motion data, is key to estimate regional Sea Ice Production rates for 1998-2020 at several "gated" Antarctic shelf embayments.

The sum of net Sea Ice Volume Transport across the outer shelf gate and the interior Sea Ice Volume change farther inshore render the Sea Ice Production Rate for that region. Most embayments, including the most important SW sources in the Ross and Weddell seas and Prydz Bay, show decreasing Sea Ice Production rates over the full

record. This partially explains the well-documented long-term freshening of SW and adjacent AABW outflows reported in those regions.

Regional timeseries of Winter Thermostad Water salinity are reconstructed from the total inputs of salt rejected by the newly-estimated Sea Ice Production rates and of meltwater from adjacent glaciers and ice shelves. In the Ross Sea a glacier meltwater input 37% higher than currently reported would halt convection intermittently after 2014. In the Southern Weddell Sea and Prydz Bay, high Sea Ice Production rates overwhelm the local freshwater inputs and result in a steadier contribution to the lower limb of the Meridional Overturning Circulation.

REFERENCES

Cavalieri, D. J., & Parkinson, C. L. (2012). Arctic sea ice variability and trends, 1979–2010. *The Cryosphere, 6*(4), 881-889.

Comiso, J. C., Kwok, R., Martin, S., & Gordon, A. L. (2011). Variability and trends in sea ice extent and ice production in the Ross Sea. *Journal of Geophysical Research: Oceans, 116*(C4).

Deacon, G. E. R. (1937). The hydrology of the Southern Ocean. *Discovery Rep., 15*, 3-122.

DeWitt, S. (2010). Ice Cloud and Land Elevation Mission Comes To An End.

Doronin, Y. P., & Kheisin, D. (1977). Sea ice.

Drucker, R., Martin, S., & Kwok, R. (2011). Sea ice production and export from coastal polynyas in the Weddell and Ross Seas. *Geophysical Research Letters, 38*(17).

Gill, A. E. (1973, 1973/02/01/). Circulation and bottom water production in the Weddell Sea. *Deep Sea Research and Oceanographic Abstracts, 20*(2), 111-140. https://doi.org/https://doi.org/10.1016/0011-7471(73)90048-X

Gordon, A. L. (2009). Bottom water formation. *Ocean Currents, 263*, 269.

Hellmer, H. H., Huhn, O., Gomis, D., & Timmermann, R. (2011). On the freshening of the northwestern Weddell Sea continental shelf. *Ocean science, 7*(3), 305-316.

Helm, K. P., Bindoff, N. L., & Church, J. A. (2010). Changes in the global hydrological-cycle inferred from ocean salinity. *Geophysical Research Letters, 37*(18).

Hendricks, S. P., S; Rinne, E. (2018a, 19/08/2021). ESA Sea Ice Climate Change Initiative (Sea_Ice_cci): Southern hemisphere sea ice thickness from the CryoSat-2 satellite on a monthly grid (LC3), v2.0. *Centre for Environmental Data Analysis*. https://doi.org/10.5285/48fc3d1e8ada405c8486ada522dae9e8

Hendricks, S. P., S; Rinne, E. (2018b, 19/08/2021
). ESA Sea Ice Climate Change Initiative (Sea_Ice_cci): Southern hemisphere sea ice thickness from the Envisat satellite on a monthly grid (L3C), v2.0. . *Centre for Environmental Data Analysis*. http://dx.doi.org/10.5285/b1f1ac03077b4aa784c5a413a2210bf5

Jacobs, S., Giulivi, C., & Mele, P. (2002). Freshening of the Ross Sea during the late 20th century. *Science, 297*(5580), 386-389.

Jacobs, S. S., Amos, A. F., & Bruchhausen, P. M. (1970). Ross Sea oceanography and Antarctic bottom water formation. Deep Sea Research and Oceanographic Abstracts,

Jacobs, S. S., & Giulivi, C. F. (2010). Large multidecadal salinity trends near the Pacific–Antarctic continental margin. *Journal of Climate, 23*(17), 4508-4524.

Johnson, G. C., Purkey, S. G., & Bullister, J. L. (2008). Warming and freshening in the abyssal southeastern Indian Ocean. *Journal of Climate, 21*(20), 5351-5363.

Kacimi, S., & Kwok, R. (2020). The Antarctic sea ice cover from ICESat-2 and CryoSat-2: freeboard, snow depth, and ice thickness. *The Cryosphere, 14*(12), 4453-4474.

Kern, S., Ozsoy-Çiçek, B., & Worby, A. P. (2016). Antarctic sea-ice thickness retrieval from ICESat: inter-comparison of different approaches. *Remote Sensing, 8*(7), 538.

Killworth, P. D. (1977). Mixing of the Weddell Sea continental slope. *Deep Sea Research, 24*(5), 427-448.

Li, H., Xie, H., Kern, S., Wan, W., Ozsoy, B., Ackley, S., & Hong, Y. (2018). Spatio-temporal variability of Antarctic sea-ice thickness and volume obtained from ICESat data using an innovative algorithm. *Remote Sensing of Environment, 219*, 44-61.

Liao, S., Luo, H., Wang, J., Shi, Q., Zhang, J., & Yang, Q. (2022). An evaluation of Antarctic sea-ice thickness from the Global Ice-Ocean Modeling and Assimilation System based on in situ and satellite observations. *The Cryosphere, 16*(5), 1807-1819.

Lindsay, R., & Zhang, J. (2006). Assimilation of ice concentration in an ice–ocean model. *Journal of Atmospheric and Oceanic Technology, 23*(5), 742-749.

Lisæter, K. A., Rosanova, J., & Evensen, G. (2003). Assimilation of ice concentration in a coupled ice–ocean model, using the Ensemble Kalman filter. *Ocean Dynamics, 53*(4), 368-388.

Martin, S., Drucker, R. S., & Kwok, R. (2007). The areas and ice production of the western and central Ross Sea polynyas, 1992–2002, and their relation to the B-15

and C-19 iceberg events of 2000 and 2002. *Journal of Marine Systems, 68*(1-2), 201-214.

Massom, R., Harris, P., Michael, K. J., & Potter, M. (1998). The distribution and formative processes of latent-heat polynyas in East Antarctica. *Annals of Glaciology, 27*, 420-426.

Massonnet, F., Mathiot, P., Fichefet, T., Goosse, H., Beatty, C. K., Vancoppenolle, M., & Lavergne, T. (2013). A model reconstruction of the Antarctic sea ice thickness and volume changes over 1980-2008 using data assimilation. *Ocean Modelling, 64*, 67-75.

Melsheimer, C. (2019). *ASI Version 5 Sea Ice Concentration User Guide*.

Morgan, B. P. (2011). *Analysis of Antarctic Sea Ice Thickness: A Newly Created Database for 2000-2009* Texas A & M University].

Mu, L., Nerger, L., Tang, Q., Loza, S. N., Sidorenko, D., Wang, Q., Semmler, T., Zampieri, L., Losch, M., & Goessling, H. F. (2020). Toward a data assimilation system for seamless sea ice prediction based on the AWI climate model. *Journal of Advances in Modeling Earth Systems, 12*(4), e2019MS001937.

NASA. (2019). *About ICESat-2*. https://www.nasa.gov/content/goddard/about-icesat-2

Nicholls, K. W., Østerhus, S., Makinson, K., Gammelsrød, T., & Fahrbach, E. (2009). Ice-ocean processes over the continental shelf of the southern Weddell Sea, Antarctica: A review. *Reviews of Geophysics, 47*(3).

Nihashi, S., & Ohshima, K. I. (2015). Circumpolar mapping of Antarctic coastal polynyas and landfast sea ice: Relationship and variability. *Journal of Climate, 28*(9), 3650-3670.

Notz, D., & Community, S. (2020). Arctic sea ice in CMIP6. *Geophysical Research Letters, 47*(10), e2019GL086749.

Orsi, A., & Webb, C. (2022). Impact of Sea Ice Production off Sabrina Coast, East Antarctica. *Geophysical Research Letters, 49*(5), e2021GL095613.

Orsi, A. H., Smethie Jr, W. M., & Bullister, J. L. (2002). On the total input of Antarctic waters to the deep ocean: A preliminary estimate from chlorofluorocarbon measurements. *Journal of Geophysical Research: Oceans, 107*(C8), 31-31-31-14.

Parkinson, C. L. (2019). A 40-y record reveals gradual Antarctic sea ice increases followed by decreases at rates far exceeding the rates seen in the Arctic. *Proceedings of the National Academy of Sciences, 116*(29), 14414-14423.

Paul, S. H., Stefan; Rinne, Eero. (2017). *D2.1 Sea Ice Thickness Algorithm Theoretical Basis Document (ATBD)* (Sea Ice Climate Change Initiative: Phase 2, Issue.

Purkey, S. G., & Johnson, G. C. (2013). Antarctic Bottom Water warming and freshening: Contributions to sea level rise, ocean freshwater budgets, and global heat gain. *Journal of Climate, 26*(16), 6105-6122.

Resti, A., Benveniste, J., Roca, M., Levrini, G., & Johannessen, J. (1999). The Envisat radar altimeter system (RA-2). *ESA bulletin, 98*(8), 94-101.

Rignot, E., Jacobs, S., Mouginot, J., & Scheuchl, B. (2013). Ice-shelf melting around Antarctica. *Science, 341*(6143), 266-270.

Rintoul, S. R. (2007). Rapid freshening of Antarctic Bottom Water formed in the Indian and Pacific oceans. *Geophysical Research Letters, 34*(6).

Schutz, B. E., Zwally, H. J., Shuman, C. A., Hancock, D., & DiMarzio, J. P. (2005). Overview of the ICESat mission. *Geophysical Research Letters, 32*(21).

Schweiger, A., Lindsay, R., Zhang, J., Steele, M., Stern, H., & Kwok, R. (2011). Uncertainty in modeled Arctic sea ice volume. *Journal of Geophysical Research: Oceans, 116*(C8).

Shi, Q., Yang, Q., Mu, L., Wang, J., Massonnet, F., & Mazloff, M. R. (2021). Evaluation of sea-ice thickness from four reanalyses in the Antarctic Weddell Sea. *The Cryosphere, 15*(1), 31-47.

Skogseth, R., Haugan, P., & Haarpaintner, J. (2004). Ice and brine production in Storfjorden from four winters of satellite and in situ observations and modeling. *Journal of Geophysical Research: Oceans, 109*(C10).

Sloyan, B. M., & Rintoul, S. R. (2001). Circulation, renewal, and modification of Antarctic Mode and Intermediate Water. *Journal of Physical Oceanography, 31*(4), 1005-1030.

Spreen, G., Kaleschke, L., & Heygster, G. (2008). Sea ice remote sensing using AMSR-E 89-GHz channels. *Journal of Geophysical Research: Oceans, 113*(C2).

Strass, V., & Fahrbach, E. (1998). Temporal and regional variation of sea ice draft and coverage in the Weddell Sea obtained from upward looking sonars. *Antarctic Sea*

Ice: Physical Processes, Interactions, and Variability (MO Jeffries, ed.), Antarctic Research Series, AGU, Washington DC, 74, 123-139.

Tamura, T., Ohshima, K. I., Fraser, A. D., & Williams, G. D. (2016). Sea ice production variability in Antarctic coastal polynyas. *Journal of Geophysical Research: Oceans, 121*(5), 2967-2979.

Tamura, T., Ohshima, K. I., & Nihashi, S. (2008). Mapping of sea ice production for Antarctic coastal polynyas. *Geophysical Research Letters, 35*(7).

Thoma, M., Jenkins, A., Holland, D., & Jacobs, S. (2008). Modelling circumpolar deep water intrusions on the Amundsen Sea continental shelf, Antarctica. *Geophysical Research Letters, 35*(18).

Tonboe, R., Lavelle, J., Pfeiffer, R.-H., & Howe, E. (2016). Product user manual for osi saf global sea ice concentration. *Danish Meteorological Institute, Denmark*.

Tonboe, R., & Nielsen, E. (2010). Global sea ice concentration reprocessing validation report. *EUMETSAT OSI SAF Prod. Rep. OSI-409, version, 1*, 18.

Tschudi, M., W. N. Meier, J. S. Stewart, C. Fowler, and J. Maslanik. . (2019). *Polar Pathfinder Daily 25 km EASE-Grid Sea Ice Motion Vectors* Version Version 4). https://doi.org/https://doi.org/10.5067/INAWUWO7QH7B.

Whitworth III, T., Orsi, A., Kim, S. J., Nowlin Jr, W., & Locarnini, R. (1998). Water masses and mixing near the Antarctic Slope Front. *Ocean, ice, and atmosphere: interactions at the Antarctic continental margin, 75*, 1-27.

Wiederwohl, C. (2012). *The Ross Sea Response to Evolving Ocean-Ice Interactions in a Changing Climate*

Willatt, R. C., Giles, K. A., Laxon, S. W., Stone-Drake, L., & Worby, A. P. (2009). Field investigations of Ku-band radar penetration into snow cover on Antarctic sea ice. *IEEE Transactions on Geoscience and remote sensing, 48*(1), 365-372.

Wong, A. P., Bindoff, N. L., & Church, J. A. (1999). Large-scale freshening of intermediate waters in the Pacific and Indian Oceans. *Nature, 400*(6743), 440-443.

Worby, A., Bush, G., & Allison, I. (2001). Seasonal development of the sea-ice thickness distribution in East Antarctica: Measurements from upward-looking sonar. *Annals of Glaciology, 33*, 177-180.

Worby, A. P., Geiger, C. A., Paget, M. J., Van Woert, M. L., Ackley, S. F., & DeLiberty, T. L. (2008). Thickness distribution of Antarctic sea ice. *Journal of Geophysical Research: Oceans, 113*(C5).

Zhang, J., & Rothrock, D. A. (2003). Modeling global sea ice with a thickness and enthalpy distribution model in generalized curvilinear coordinates. *Monthly Weather Review, 131*(5), 845-861.

APPENDIX A

QUALITY CONTROL OF NIC CHART DATA DURING SIT COMPUTATION

A.1. Missing stage of development and/or partial concentration

NIC ice charts are created by analysts using multiple remote sensing sources to determine regions with similar ice features. They trace polygons around those regions and identify the stages of development and partial concentrations of the various ice types within. At times, due to source data limitations, not all features could be identified. Missing data in the NIC charts are flagged with a 99 value and occur for two reasons: 1. there are two or more ice types and S is identified but C is missing; 2. There are one or more ice types and C is identified but S is missing. Scenario 1 occurs most frequently because complete coverage of a polygon region is necessary to determine the partial concentrations of all ice types within, while incomplete coverage can still allow identification of the different ice types.

Missing Sa-d and Ca-d data were filled in different ways. Since the interannual variability of Antarctic sea ice characteristics is much lower than their seasonal variability, missing Sa-d data of any given month are filled with the data average of the same month in the closest years. For example missing data in April, 2005 would be filled with the average of April values during 2004-2006. However, at many grid points in the early 2000s there were multiple consecutive years with missing Ca-d values for which this method proved ineffective. These pervasive missing Ca-d values were instead filled

with record length monthly averages. For example missing Ca-d in April 2005 would be filled with the average of values during all Aprils.

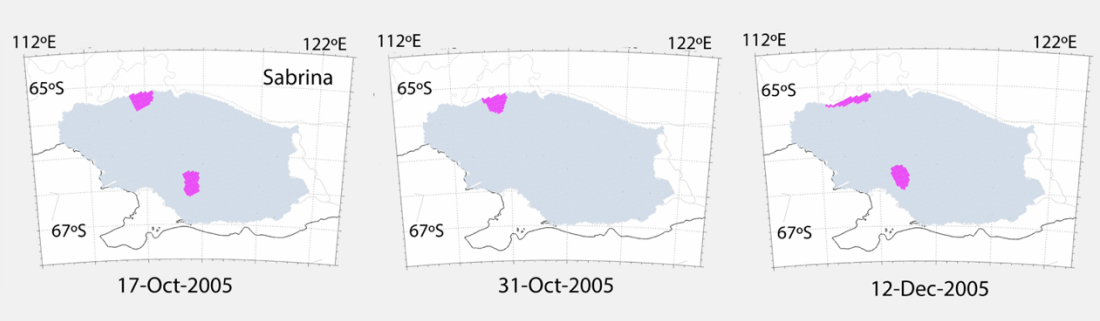

Figure 22. An example of an iceberg in the Sabrina Basin that was not traced for three weeks during October-November 2005. In this case we replaced the iceberg during the first two missing records with its location from 17-Oct-2005 and in the last missing record with its location from 12-Dec-2005.

A.2. Iceberg continuity

Icebergs are not sea ice and thus no sea ice thickness should be assigned to grid points covered buy them. Icebergs appear in the NIC charts as polygons in which the only ice type is "glacier ice" (SIGRID S: 98) away from the coast. When 98 is used near the coast it describes glaciers and ice shelves. Iceberg tracing began in 2003 so the first 5 years of charts do not identify them. Periodically icebergs vanished, often reappearing one or more weeks later. In Figure 22 an iceberg in the Sabrina sector was traced until the 17th of October, 2005 after which is was absent for three charts reappearing on the 12th of December. If left uncorrected this creates an artificial increase in SIV when the iceberg vanishes followed by a decrease in SIV when it returns. This would skew the weekly variability in SIP by artificially adding to or subtracting from the ΔSIV term. If

icebergs do not reappear they are assumed to have been transported from the sector, a common occurrence since icebergs often move through a sector in just a few weeks. If they do reappear they are filled in the grid points where they were last seen. If icebergs are missing for multiple weeks, the first half are filled with the location of the last observation and the latter half in the location where the iceberg first reappears. In the example from Figure 22, the iceberg was replaced in the first two missing records with its location on the 17th of October and filled in the last missing record with its location on the 12th of December. Some semi-stationary icebergs were found in the first weeks of iceberg tracing and were projected back to the start of the dataset with the assumption that the iceberg did not moved during that time. For example, iceberg A-23A in the Southern Weddell (Figure 23) which calved in 1986 was not continuously traced before March 2004. We replaced A-23A in all early charts using its location on the 2nd of May, 2005.

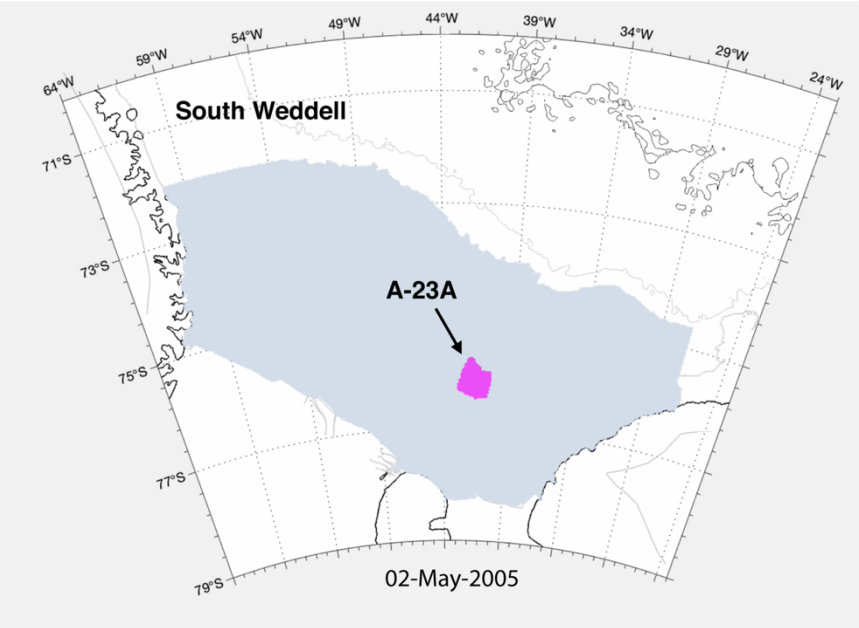

Figure 23. Iceberg A-23A calved in 1986 in the South Weddell Sea and has moved little since grounding in the location shown here. A-23A was missing before March 2004 in the ice charts and was replaced in this location for all earlier records.